ACS OMEGA

Open Access

http://pubs.acs.org/journal/acsodf

Article

Novel Phosphoric Acid-Modified Biochar−Chitosan Nanocomposite for an Efficient and Cost-Effective Multimetal Removal from Wastewater

Khandgave Santosh Sopanrao and Inkollu Sreedhar*

Cite This: https://doi.org/10.1021/acsomega.5c04698

Read Online

ACCESS | Metrics & More | Article Recommendations | Supporting Information

ABSTRACT: This study presented a novel and cost-effective adsorbent developed from phosphoric acid-modified biochar−chitosan nanocomposite for the efficient removal of Cu^{2+}, Ni^{2+}, and Zn^{2+} from wastewater. The biochar was synthesized at an optimized pyrolysis temperature of 550 °C for 2 h, followed by modification with phosphoric acid and composed of chitosan, resulting in a mesoporous PGB−CS composite (9.18 nm pore diameter) that exhibited a high surface area (167.98 m^2/g), low crystallinity, good thermal stability, and abundant surface functional groups such as amine, carboxylic, and hydroxyl. The adsorption parameters were optimized using the Box−Behnken design of response surface methodology, obtaining maximum adsorption capacities of 221.56 mg/g for Cu^{2+}, 175.47 mg/g for Ni^{2+}, and 127.46 mg/g for Zn^{2+} under optimal conditions. The pH study further improved the adsorption capacities to 249.78 mg/g for Cu^{2+}, 191.48 mg/g for Ni^{2+}, and 145.91 mg/g for Zn^{2+}. The adsorption process followed pseudo-second-order kinetics, indicating chemisorption, and confirmed the Langmuir isotherm, suggesting monolayer adsorption. Thermodynamic parameters confirmed the spontaneous and endothermic nature of the adsorption. Real industrial effluent from a battery manufacturing industry demonstrated removal efficiencies of 83.19% (Cu^{2+}), 61.94% (Ni^{2+}), and 52.34% (Zn^{2+}). The adsorbent maintained stability and reusability over 8 regeneration cycles, with desorption efficiencies of 53.17%, 51.97%, and 51.07% for Cu^{2+}, Ni^{2+}, and Zn^{2+}, respectively, using H_2SO_4, HNO_3, and HCl. The synthesis cost was estimated as USD 8.13/g (Rs. 682.14/g), indicating strong economic potential. Adsorption mechanisms were attributed to surface complexation, ion exchange, and electrostatic attraction. The developed adsorbent provided a sustainable and efficient approach for treating heavy-metal-contaminated industrial wastewater.

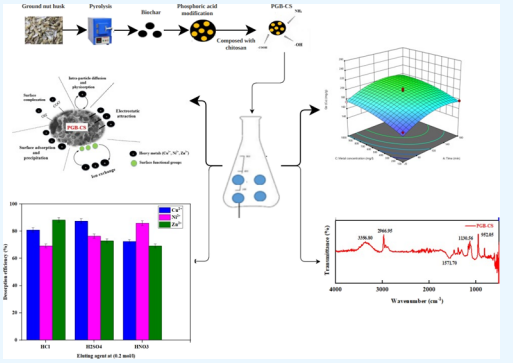

1. INTRODUCTION

The presence of heavy metals in wastewater beyond permissible limits has significant consequences on human health and aquatic ecosystems. Exposure to such contaminants leads to serious health problems, including neurological disorders, kidney damage, and cancer.[1] Therefore, it was essential to adopt sustainable and cost-effective technologies to mitigate heavy metal contamination in industrial wastewater and safeguard both public health and the environment.[2,3] The various treatment methods such as membrane filtration, ion exchange, electrocoagulation, adsorption, etc., were employed to address heavy metal removal from wastewater.[4,5] Among these, adsorption emerged as the most widely used technique due to its economic viability, low sludge generation, and ease of regeneration.[6] Adsorption involves the accumulation of contaminants onto the surface of solid adsorbents via physical or chemical interactions, and its performance is largely influenced by factors such as surface area, pore structure, surface charge, and the presence of functional groups.[7−11] Chitosan, derived from chitin, offered several advantages including biodegradability, nontoxicity, and the presence of abundant functional groups (−OH, −COOH, $-NH_2$) along its polymer backbone, making it a promising candidate for heavy metal adsorption.[12] However, due to its high crystallinity and limited mechanical strength, chitosan often required chemical modification or blending with other materials to enhance its adsorption efficiency.[13]

Several studies have investigated the use of chitosan-based composites for the removal of heavy metals from an aqueous solution. A poly(acrylic acid)-modified chitosan−biochar composite has demonstrated excellent adsorption performance and achieved adsorption capacities of 111.11 mg/g for Cu^{2+}, 114.94 mg/g for Zn^{2+}, 99.01 mg/g for Ni^{2+}, 476.19 mg/g for Pb^{2+}, 370.37 mg/g for Cd^{2+}, 138.89 mg/g for Mn^{2+}, 135.14 mg/g for Co^{2+}, and 312.50 mg/g for Cr^{3+}. These results were

Received: May 19, 2025
Revised: August 21, 2025
Accepted: September 4, 2025

obtained largely due to the surface complexation facilitated by carboxyl and hydroxyl functional groups from poly(acrylic acid) and chitosan, as well as the porous structure of the biochar, which improved mass transfer and ion diffusion.[14] Similarly, a carbonized zeolite/chitosan composite synthesized by pyrolysis at 500 °C exhibited adsorption capacities of 111.35 mg/g for Cu^{2+} and 104.75 mg/g for Cr^{6+}. The strong performance was observed at pH 8.1 for Cu^{2+} and 9.6 for Cr^{6+} removal facilitated by ion-exchange and chemisorption mechanisms.[15] Additionally, a chitosan−polyethylene glycol composite effectively removed cadmium and achieved an adsorption capacity of 265 mg/g;[16] a nitrogen-doped chitosan-ferric adsorbent attained an adsorption capacity of 183.85 mg/g for Cu^{2+} removal with chemisorption on a monolayer surface, which was the dominant mechanism.[17] Porous carboxymethyl chitosan beads demonstrated Co^{2+} removal with an adsorption capacity of 46.25 mg/g, primarily driven by the surface complexation and electrostatic interactions.[18] The introduction of carboxymethyl groups has increased the negative surface charge and improved the affinity toward the divalent metal ions.[18] A chitosan material grafted with hydroxyethyl methacrylate and acrylic acid showed a Cu^{2+} adsorption capacity of 156.49 mg/g at a 1000 mg/L initial metal concentration and 4.5 g/L dosage.[19] The formation of a chelating network involving the hydroxyl and carboxylic groups on the grafted chains contributed to strong metal binding affinity.[19] In another study, arginine-functionalized magnetic chitosan nanoparticles achieved 83.25 mg/g for Ni^{2+} removal at a 100 mg/L metal ion concentration using a 6 g/L dosage.[20] This was due to the high surface area of nanoparticles and the presence of amine and carboxyl groups from arginine, which promoted rapid adsorption via electrostatic interaction and coordination bonding.[20] Similarly, the chitosan−biochar composite removed Zn^{2+} with an adsorption capacity of 117.50 mg/g under optimal pH and dosage conditions.[21] The high performance was attributed to the synergistic interaction between the amine groups of chitosan and the microporous structure of biochar, which facilitated ion exchange and surface adsorption.[21]

Phosphoric acid-modified chitosan adsorbents have been increasingly studied for their enhanced performance in heavy metal remediation. For example, phosphoric acid-modified bentonite−chitosan composite beads achieved adsorption capacities of 362.24 mg/g for Cu^{2+}, 279.51 mg/g for Ni^{2+}, and 210.54 mg/g for Zn^{2+} removal from an aqueous solution.[22] The high adsorption capacity confirmed the composite's practical viability, with phosphate and amine functional groups providing multiple active binding sites for metal ions.[22] Similarly, a phosphorus-modified corn biochar significantly enhanced the adsorption performance, achieving maximum capacities of 145.48 mg/g for Pb^{2+} and 14.53 mg/g for Cd^{2+}, which were 6.46 times and 3.67 times higher than those of the unmodified biochar.[23] This improvement was attributed to the introduction of phosphate functional groups, which increased surface acidity and created additional active binding sites for metal ions. In another study, coconut shell carbon was modified with chitosan and an oxidizing agent (phosphoric acid) to produce a composite adsorbent, achieving a Zn^{2+} adsorption capacity of 60.41 mg/g.[24] The enhanced performance was attributed to the availability of active sites for metal ion binding through surface complexation, electrostatic attraction, and ion-exchange mechanisms. Similarly, a simple and cost-effective method was employed to synthesize single-calcium-atom biochar-supported nanoscale zerovalent iron composites using shrimp shell biomass for the efficient removal of tris(2-chloroethyl) phosphate through Fenton-like oxidation.[25] Under the optimized conditions, the system achieved rapid adsorption and complete degradation of the contaminant within 30 min, exhibiting notable stability across a broad pH range. In a related study, a poly(vinyl alcohol)-anchored L-cysteine composite was utilized for the removal of heavy metals such as Hg, Cr, Pb, and Cd from wastewater, displaying maximum adsorption capacities of 48.5, 25.0, 45.25, and 44.25 mg/g, respectively.[26] The adsorption followed the Langmuir isotherm and pseudo-first-order kinetic model, and effective regeneration was achieved using nitric acid. Furthermore, olive pit-derived activated carbon was assessed as an adsorbent for methylene blue removal, where activation using phosphoric acid proved more effective than sulfuric acid.[27] The optimal performance was observed at a particle size of 0.6 mm, a temperature of 30 °C, and an alkaline pH (∼8), with equilibrium attained within 60−120 min. Additionally, a poly(vinyl alcohol)-based composite functionalized with L-2-amino-3-mercaptopropionic acid showed efficient adsorption of Hg^{2+}, Cr^{3+}, Pb^{2+}, and Cd^{2+}, with adsorption capacities reaching up to 49.6 mg/g under mild conditions (pH 4−5.5, room temperature, and 15−20 min contact time).[28]

These studies have demonstrated that phosphoric acid-modified biochar−chitosan composites offered several benefits including easy synthesis, enhanced surface area, various metal ion binding capabilities, and cost-effectiveness, making it a promising adsorbent for heavy metal removal from wastewater.[29] The limited studies investigated the application of various adsorbents for the treatment of real industrial effluents. For example, phosphoric acid-modified bentonite−chitosan composite beads were used to treat battery manufacturing effluent and achieved removal efficiencies of 88.59% for Cu^{2+}, 72.30% for Ni^{2+}, and 62.07% for Zn^{2+} using an adsorbent dosage of 1 g/L and a contact time of 30 min.[22] Similarly, rice husk, an untreated agricultural byproduct, exhibited relatively low removal efficiencies of 24.49% for Cu^{2+} and 37.38% for Ni^{2+} from industrial wastewater, which was attributed to its limited number of active sites and low surface reactivity.[30] In contrast, fly ash, a byproduct of coal combustion rich in aluminosilicates, demonstrated significantly higher removal efficiencies of 94.88% for Cu^{2+} and 94.54% for Ni^{2+} from industrial wastewater due to its high surface area, porosity, and ion-exchange capacity.[30] In another study, poly(vinyl alcohol)-modified chitosan was used to treat battery effluent and resulted in removal efficiencies of 79.09% for Cu^{2+}, 50.73% for Ni^{2+}, and 46.90% for Zn^{2+}, highlighting the effectiveness of surface functionalization in enhancing metal ion binding.[31] A wood sawdust was used to treat electroplating wastewater, achieving a 38.3% removal of Cu^{2+} and 14.0% of Zn^{2+}, indicating that it has limited adsorption performance for the treatment of industry wastewater.[32] Similarly, magnesium oxide nanoparticles have removed 70.80% of Ni^{2+} from textile and tannery effluents, which was attributed to their high surface reactivity and strong electrostatic interactions with the divalent metal ions.[33] These findings emphasized the importance of adsorbent selection and surface modification strategies to enhance the treatment efficiency of heavy metals in real industrial wastewater.

In the existing literature, most of the studies have focused on the removal of a single heavy metal from aqueous solution using various adsorbents, with limited attention given to the

https://doi.org/10.1021/acsomega.5c04698
ACS Omega XXXX, XXX, XXX−XXX

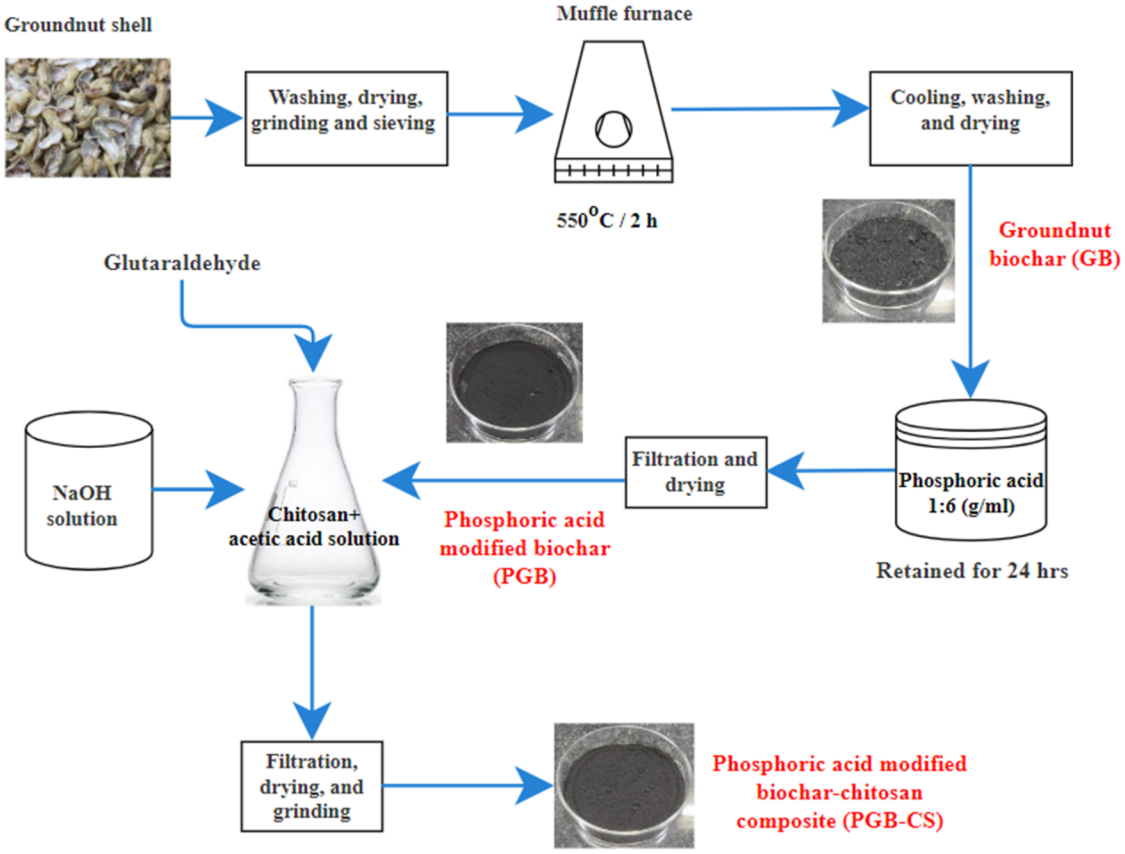

Figure 1. Synthesis method of the PGB−CS adsorbent.

simultaneous multimetal removal from both aqueous and real industrial wastewaters. This study addressed this gap by developing a novel phosphoric acid-modified groundnut (*Arachis hypogaea*) shell biochar−chitosan composite (PGB−CS) and evaluated its performance using a systematic three-level optimization approach. In the first level, biochar synthesis conditions (pyrolysis temperature and pyrolysis time) were optimized to obtain favorable surface properties. In the second level, process variables such as contact time, metal concentration, and adsorbent dosage were optimized using response surface methodology (RSM). In the third level, pH was optimized and validated through a point of zero charge (pH_{pzc}). Although many adsorption studies have focused on pseudo-first-order (PFO) and pseudo-second-order (PSO) kinetic models, along with Langmuir, Freundlich, and Temkin isotherms, the present study adopted a more comprehensive modeling approach. In addition to the PFO and PSO models, the kinetic data were evaluated using the Elovich and Weber−Morris (intraparticle diffusion) models to gain further insight into the adsorption mechanism. Similarly, the adsorption equilibrium was analyzed using Dubinin−Radushkevich (D−R), Jovanovic, and Harkins−Jura (H−J) isotherm models, in addition to the commonly applied Langmuir, Freundlich, and Temkin models. In addition, thermodynamic analysis confirmed that the adsorption process was spontaneous, feasible, and endothermic in nature. The adsorption of heavy metals using PGB−CS was primarily governed by surface complexation, electrostatic attraction, and ion-exchange mechanisms. Many studies evaluated regeneration only up to three cycles, whereas this study demonstrated that PGB−CS was effective up to eight regeneration cycles. Furthermore, the adsorbent exhibited a low production cost of USD 8.13/g (Rs. 682.14/g), making it a cost-effective and practical candidate for industrial-scale wastewater decontamination.

2. MATERIALS AND METHODS

2.1. Materials. Groundnut (*A. hypogaea*) shell, selected for its lignocellulosic composition and carbon-rich framework, was procured from a local market in Hyderabad, India. It served as the precursor for biochar synthesis aimed at the efficient removal of heavy metals from aqueous and industrial wastewaters. The chemicals used in this study included phosphoric acid (85% extra pure), copper chloride (98% pure), zinc chloride (97% assay), nickel nitrate hexahydrate (98% pure), sodium hydroxide pellets (97% assay), and high molecular chitosan, which were purchased from Sisco Research Laboratories (SRL, India). Nitric acid (69−72% assay) was obtained from Qualigens, glutaraldehyde was obtained from Otto Chemik, hydrochloric acid (36.5−38% pure) was obtained from Finar, and H_2SO_4 (98% assay) and CH_3COOH (99.5% assay) were obtained from SDFCL. Real industrial wastewater containing a mixture of heavy metals was sourced from HBL Power Systems Limited, Hyderabad, India, to assess the field applicability of the synthesized adsorbent.

2.2. Synthesis Method of PGB−CS. Groundnut (*A. hypogaea*) shell was initially washed, dried, ground, and sieved to a particle size range of 75−150 μm. Pyrolysis was carried out in a muffle furnace (LK Lab, LF-MS230, Korea) at a temperature of 550 °C for 2 h in an earthen pot setup. This temperature and time combination was selected based on the first-level optimization results that yielded the best structural and adsorption properties.[13] The product was allowed to cool

https://doi.org/10.1021/acsomega.5c04698
ACS Omega XXXX, XXX, XXX−XXX

Table 1. List of Adsorption Isotherms and Kinetic Models

isotherm/kinetic model	nonlinear form	notations
Langmuir isotherm	$q_e = \frac{K_L q_m C_e}{1 + K_L C_e}$ and $R_L = \frac{1}{1 + K_L C_i}$	q_e: equilibrium adsorption capacity (mg/g); q_m: maximum adsorption capacity (mg/g); R_L: separation factor; K_L: Langmuir constant (L/mg); C_i: adsorbate initial concentration (mg/L)
Freundlich isotherm	$q_e = K_F C_e^{1/n}$	K_F and $1/n$ are the Freundlich constants
Temkin isotherm	$q_e = \frac{RT}{b_T}\ln(K_T C_e)$	R: Universal gas constant (8.314 J mol^{-1} K^{-1}); T: temperature (K); b_T: Temkin constant related to the heat of adsorption (J/mol); K_T: Temkin equilibrium binding constant (L/mg); C_e: equilibrium metal concentration (mg/L)
Dubinin–Radushkevich (D–R) isotherm	$q_e = q_m \exp(-\beta\varepsilon^2)$ where, $\varepsilon = RT\ln\left(1 + \frac{1}{C_e}\right)$; $E_a = \frac{1}{\sqrt{2\beta}}$	β: D–R constant related to the adsorption energy (mol^2/kJ^2); ε: Polanyi potential (kJ/mol); E_a: mean free energy of adsorption (kJ/mol)
Jovanovic isotherm	$q_e = q_m(1 - \exp(K_j C_e))$	K_j: Jovanovic constant (L/mg)
Harkins–Jura (H–J) isotherm	$q_e = \sqrt{\frac{A_{HJ}}{B_{HJ} - \ln(C_e)}}$	B_{HJ} and A_{HJ} (mg/g)^2 are Harkins–Jura constants
Pseudo-first order	$q_t = q_e(1 - \exp(-k_1 t)$	q_t: time-dependent adsorption capacity (mg/g); k_1: equilibrium rate constant in (min^{-1})
Elovich model	$q_t = \frac{1}{\beta}\ln(1 + \alpha\beta t)$	α: rate related to the initial adsorption (mg g^{-1} min^{-1}); β: constant to desorption (g·mg)
Weber and Morris (Intraparticle diffusion model)	$q_t = k_{W\&M}\sqrt{t} + C$	$k_{W\&M}$: constant concerning the diffusion rate (mg/g·min$^{-1/2}$), C is the intercept constant (mg/g)

naturally for 10 h and was referred to as groundnut (*A. hypogaea*) shell biochar (GB). To enhance surface functionality and porosity, GB was modified using phosphoric acid.[34] It was mixed with H_3PO_4 in a 1:6 (g/v) ratio and kept there for 24 h. The mixture was then filtered, washed multiple times to neutralize, and dried to obtain phosphoric acid-modified groundnut (*A. hypogaea*) shell biochar (PGB). Separately, chitosan (CS) was dissolved in a 3% (v/v) CH_3COOH (3 mL in 100 mL of water) solution at 2 g per 100 mL and stirred at 220–230 rpm for 8 h to form a uniform gel. Further, PGB was added to the chitosan solution in a 3:1 ratio and stirred for 1 h to ensure uniform dispersion. The addition of 3.0 mL of glutaraldehyde improved the mechanical stability of the composite via cross-linking.[22] The resulting gel was precipitated in 3% w/v NaOH (3.0 g in 100 mL water) solution, followed by filtration, washed multiple times, dried, and ground to form the final composite as a phosphoric acid-modified groundnut (*A. hypogaea*) shell biochar–chitosan (PGB–CS). A schematic of the synthesizing process is presented in Figure 1.

2.3. Characterization Methods. The characterization of the adsorbent and sample analysis was examined using various analytical techniques. Atomic absorption spectroscopy (AAS) was conducted using a Shimadzu AA-7000 (Japan) equipment to quantify the concentration of metal ions before and after adsorption. Thermogravimetric analysis (TGA) was performed on a Shimadzu DTG-60 (Japan) equipment to evaluate the thermal stability and decomposition behavior of the material. The specific surface area and pore characteristics were determined using the Brunauer–Emmett–Teller (BET) method with a Microtrac Bel BEL SORP mini II (Japan) equipment. Functional groups present on the adsorbent surface were identified using a Fourier transform infrared spectrometer (FTIR) (Jasco-4200, Japan). Morphological features were examined through field emission scanning electron microscopy (FE-SEM) using an FEI Apreo LoVac (USA), and elemental composition was analyzed via energy-dispersive X-ray spectroscopy (EDX) using Oxford Instruments (England). The surface chemical states and elemental bonding environments were characterized using X-ray photoelectron spectroscopy (XPS) using a Thermo Fisher Scientific K-α instrument (UK). Additionally, the crystalline structure of the material was investigated using X-ray powder diffraction (XRD) on a Rigaku ULTIMA-IV (Japan).

2.4. Experiments. To experimentally validate the adsorptive performance of the PGB–CS adsorbent, a multistage approach was undertaken. In the first level of optimization, pyrolysis of groundnut (*A. hypogaea*) biomass (GB) was carried out in a controlled muffle furnace within a temperature range of 500–600 °C. The purpose was to determine the optimum pyrolysis temperature that yields the highest adsorption capacity (q_e). Once the optimal temperature (550 °C) was identified, a time-based study was performed in the range of 1–3 h to evaluate the influence of the pyrolysis time on q_e. The mathematical expressions used to calculate the adsorption capacity (q_e) and removal efficiency (R) were calculated using eqs 1 and 2, respectively

$$q_e = \frac{(C_i - C_0)V}{m} \tag{1}$$

$$R = \frac{(C_i - C_0)}{C_i} \times 100 \tag{2}$$

Here, C_i (mg/L) and C_0 (mg/L) are the initial and final metal concentrations, respectively, V is the solution volume (L), and m (g) is the adsorbent mass.

In the second level of optimization, a statistical approach using response surface methodology (RSM) was employed to fine-tune the adsorption parameters. Using Design-Expert 13.0 software, 17 experimental runs were designed by varying the adsorbent dosage (1–10 g/L), contact time (20–180 min), and initial metal concentration (100–1000 mg/L). The aim was to maximize the adsorption capacity (q_e) by optimizing conditions with minimal contact time and adsorbent dosage while handling a high initial metal concentration. The RSM optimized conditions were identified as a 1000 mg/L metal concentration, 36 min batch time, and 1 g/L of adsorbent dosage for Cu^{2+}, and 20 min batch time, 1000 mg/L metal concentration, and 1 g/L adsorbent dosage for both Ni^{2+} and Zn^{2+}, respectively. Isotherm experiments were subsequently conducted to describe the equilibrium behavior of heavy metal

https://doi.org/10.1021/acsomega.5c04698
ACS Omega XXXX, XXX, XXX–XXX

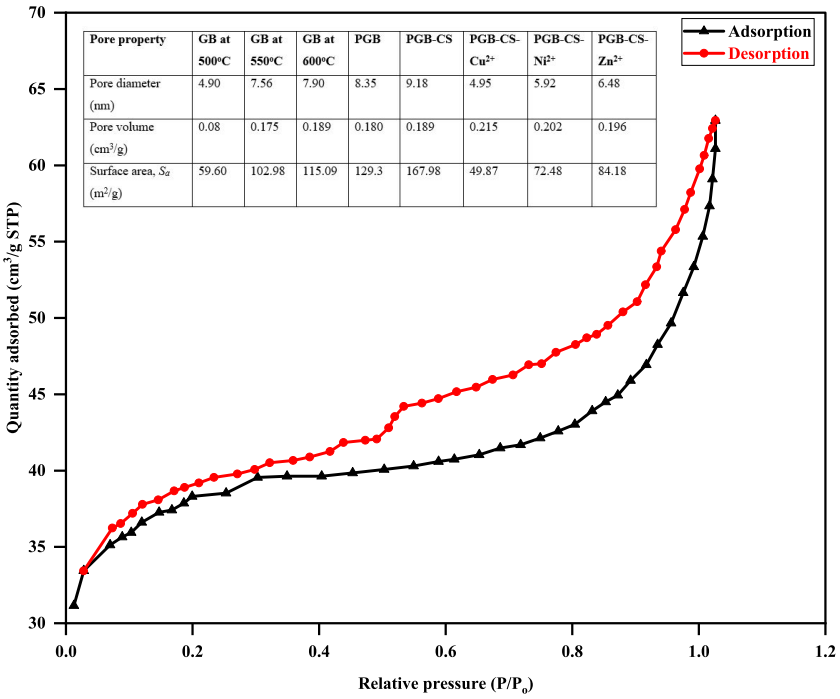

Pore property	GB at 500°C	GB at 550°C	GB at 600°C	PGB	PGB-CS	PGB-CS-Cu^{2+}	PGB-CS-Ni^{2+}	PGB-CS-Zn^{2+}
Pore diameter (nm)	4.90	7.56	7.90	8.35	9.18	4.95	5.92	6.48
Pore volume (cm^3/g)	0.08	0.175	0.189	0.180	0.189	0.215	0.202	0.196
Surface area, S_a (m^2/g)	59.60	102.98	115.09	129.3	167.98	49.87	72.48	84.18

Figure 2. Adsorption−desorption isotherm of the PGB−CS adsorbent.

adsorption. These were performed at the RSM optimum conditions with varying metal concentrations from 100 to 1500 mg/L. The experimental data was fitted to six different nonlinear isotherm models to determine the best one. Similarly, kinetic studies were performed at fixed metal concentrations of 1000 and 1 g/L adsorbent dosages under RSM optimum conditions, with sampling done at time intervals ranging from 10 to 100 min. Furthermore, experimental data was attempted to fit with the four kinetic models. The list of isotherms and kinetic models used in this study is given in Table 1.

Each batch experiment was conducted in triplicate to ensure reliability, and average values were reported. The associated error analysis, including the standard deviation (σ), was computed. The σ was determined using eq 3

$$\sigma = \sqrt{\frac{\sum_{i=1}^{n} (x_i - \overline{x})^2}{N}} \quad (3)$$

Here, x_i is the individual data value, $\overline{x}$ is the average value, and N is the number of data values.

In the third level of optimization, the effect of pH on the adsorption capacity of Cu^{2+}, Ni^{2+}, and Zn^{2+} was studied over a pH range of 2.0−6.0. The point of zero charge (pH_{pzc}) was determined by using a mass titration method in 0.1 mol/L of $NaNO_3$ across the same pH range. To assess selective adsorption, a ternary mixture containing 200 mg/L of each metal ion was treated under batch conditions (pH 5.0, 1 g/L dosage, and 20 min contact time), and individual q_e values were determined for each metal ion. Furthermore, the applicability of the adsorbent was validated using real industrial effluent obtained from a battery manufacturing unit. The effluent was treated using a 1 g/L dosage for 20 min, and the adsorption capacity was evaluated. Finally, the regeneration potential of the adsorbent was assessed using three eluents: HCl, H_2SO_4, and HNO_3 at concentrations between 0.1 and 1 mol/L. The best-performing eluent for each metal ion was identified based on the maximum desorption efficiency (R_{des}). Subsequently, cyclic adsorption−desorption experiments were conducted for up to eight cycles for each metal: Cu^{2+} (0.4 mol/L H_2SO_4), Ni^{2+} (0.6 mol/L HNO_3), and Zn^{2+} (0.6 mol/L HCl), and R_{des} values were recorded to confirm the reusability and stability of the adsorbent over multiple cycles.

3. RESULTS AND DISCUSSION

3.1. Comprehensive Characterization of Adsorbent.

3.1.1. Surface Area Analysis. The adsorbent samples were degassed at 200 °C for 2 h under vacuum to remove any moisture or volatile contaminants. Nitrogen gas was then used as the adsorbate, and the adsorption−desorption isotherms were recorded at 77 K as presented in Figure 2. The specific surface area was determined using the BET method, and pore characteristics were derived from the isotherm data. The adsorption/desorption isotherm demonstrated to the type-II class of the IUPAC classification, indicating the presence of micro- and mesoporoes.[35] At low relative pressure (0.012−0.25), micropores were predominantly filled initially, implying monolayer adsorption. As the pressure increased, multilayer adsorption succeeded, resulting in the formation of additional layers of N_2 on the surface. Further elevation in the relative pressure suggested a N_2 condensation within the mesoporous material with varying pore diameters.[31] However, at a relative pressure of 0.49, the adsorption and desorption processes were nonreversible. A divergence between the adsorption and desorption curves was observed between relative pressures of 0.5 and 0.99. This disparity may indicate the presence of a complex pore structure within the material, characterized by different pore sizes or shapes, leading to variations in the N_2 uptake and release.[36] A similar isotherm pattern was observed in heavy metal removal using an agriculture waste-derived biochar and chitosan composite.[37] Similarly, the pore characteristics of GB were assessed at three pyrolysis temperatures: 500 °C, 550 °C, and 600 °C, to determine the

https://doi.org/10.1021/acsomega.5c04698
ACS Omega XXXX, XXX, XXX−XXX

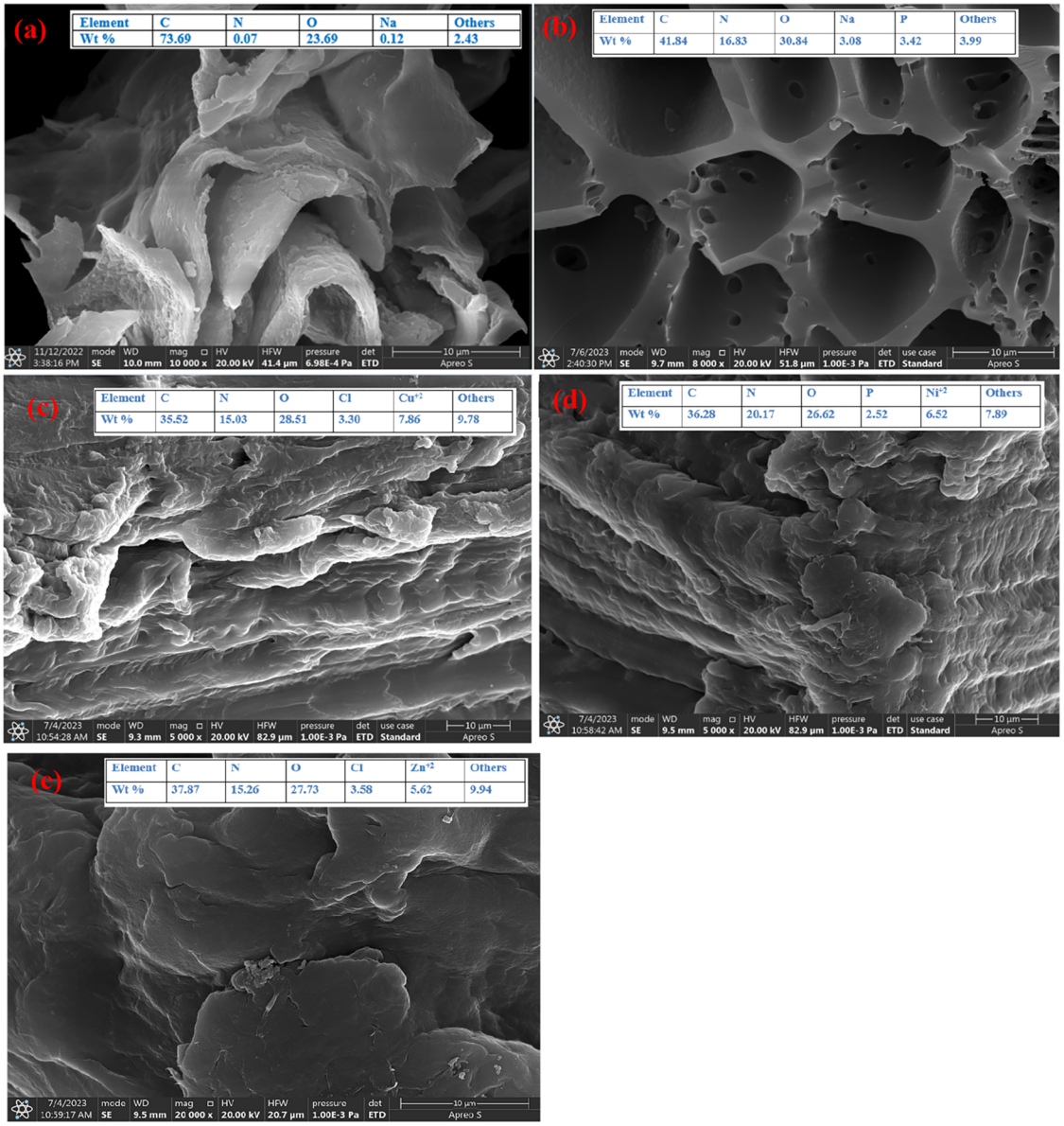

Figure 3. SEM and EDX results of PGB−CS: (a) GB, (b) PGB−CS, (c) PGB−CS−Cu^{2+}, (d) PGB−CS−Ni^{2+}, and (e) PGB−CS−Zn^{2+}.

most suitable condition as presented in Figure 2. The increase of 54.28% in the pore diameter (4.90−7.56 nm) and 72.78% in the surface area (59.60−102.98 m^2/g) from 500 to 550 °C was observed. However, the increase was less observed, only 4.49% in pore diameter (7.56−7.90 nm) and 11.75% in surface area (102.98−115.09 m^2/g) from 550 to 600 °C, respectively. Therefore, choosing a pyrolysis temperature of 550 °C was considered a reasonable compromise, balancing improved adsorption characteristics with energy consumption. The surface area was increased from 102.98 m^2/g (GB) to 167.98 m^2/g (PGB−CS), which indicated improved porosity due to chemical treatment. Similarly, the total pore volume was increased from 0.175 cm^3/g to 0.189 cm^3/g, and the average pore diameter expanded from 7.56 to 9.18 nm. A decrease in pore diameter by 46.07% (9.18−4.95 nm), 35.51% (9.18−5.92 nm), and 29.41% (9.18−6.48 nm) was observed after the adsorption of Ni^{2+}, Zn^{2+}, and Cu^{2+}, respectively. This suggests that the metal ions filled the pores and created a coating on the surface.[38] The trend of change in pore properties after metal adsorption aligned with the reported studies for the heavy metal removal using chitosan and its composites.[21,31,39] A comparison of surface properties with the reported studies in the literature is presented in Table S1.

3.1.2. Surface Morphology and Elemental Analysis. For SEM imaging, small quantities of adsorbent samples were mounted onto aluminum stubs by using carbon tape. The surface morphology of both pristine and metal-loaded PGB−CS was examined using SEM operated at an accelerating voltage of 5−15 kV, and morphologies are presented in Figure 3. Elemental composition and distribution were analyzed using EDX, performed at three distinct surface points on each sample, and the average values were compiled and are presented in Table S2. The EDX analysis of the biochar (GB) showed a high carbon content (73.69 wt %), oxygen (23.69 wt %), and negligible nitrogen (0.07 wt %), as presented in Figure 3a, whereas for the PGB−CS sample, the dominant elements were carbon (41.84 wt %), oxygen (30.84 wt %), and nitrogen (16.83 wt %), which originated from the biochar and chitosan components. The reduction in carbon and nitrogen contents after heavy metal adsorption suggested

https://doi.org/10.1021/acsomega.5c04698
ACS Omega XXXX, XXX, XXX−XXX

effective binding of heavy metal ions onto the surface of PGB−CS through interactions with its functional groups.[21] Before metal adsorption, as presented in Figure 3b, a porous surface was revealed, which was due to the evaporation of moisture during the drying stage. Additionally, the presence of phosphorus was detected (3.42% by weight) before the adsorption, which was attributed to the H_3PO_4 modification of the biochar. After metal ion adsorption, the phosphorus content was reduced to 2.56, 2.52, and 2.74 wt % after Cu^{2+}, Ni^{2+}, and Zn^{2+} adsorption, respectively as presented in Table S2. This modification resulted in the formation of phosphate ($-PO_4^{3-}$) and phosphite ($-PO_3^{3-}$) bonds, which enhanced the stability of the carbon structure and improved metal adsorption.[40] After metal adsorption, the pores were filled by metal ions, resulting in a film-like surface, as shown in Figure 3c,d,e. The EDX analysis further observed weight percentages of 7.86% for Cu^{2+}, 6.52% for Ni^{2+}, and 5.62% for Zn^{2+} after adsorption, suggesting that effective metal adsorption occurred on the PGB−CS surface. Similar surface morphologies have been reported in the previous studies for the mitigation of heavy metals using a poly(acrylic acid)-modified chitosan−rice straw biochar composite,[14] poly(vinyl alcohol)-modified chitosan,[31] phosphoric acid-modified bentonite−chitosan composite beads,[22] and chitosan−magnetic biochar composite.[21]

3.1.3. Thermal Stability. A known weight of the sample was loaded into a platinum crucible for thermogravimetric analysis. The analysis was conducted under a nitrogen atmosphere from room temperature to 1000 °C at a constant heating rate of 15 °C/min. The weight loss profile was recorded to evaluate thermal degradation and stability of the adsorbent before and after the adsorption of metal ions. TGA and DTG analyses of PGB−CS before and after adsorption of metal ions are shown in Figure S1a,b. Initially, there was a gradual weight loss of 15.57%, occurring until the temperature reached 186.02 °C. The removal of moisture at this stage was crucial for preparing the material for subsequent thermal processes. Following this, a substantial weight loss of 43.57% occurred between 186.02 and 444.77 °C, representing the second stage of degradation. Finally, a weight loss of 13.58% was observed in the last stage. The initial weight loss was likely attributed to the evaporation of physically adsorbed moisture and volatile compounds.[34] The second stage of weight reduction signified the depolymerization and removal of functional groups like amines, carboxyls, hydroxyls, etc.[31] The substantial weight loss during this stage suggested more significant chemical and structural changes within the composite material. Finally, the weight reduction in the final phase was linked to the thermal decay of residues remaining from the previous stage, indicating a more advanced breakdown of PGB−CS, ultimately forming carbons and hydrocarbons.[2] A noticeable pattern of reduced weight loss was observed following adsorption. This effect was due to the metal deposition within the microspores, forming a protective layer that restricted metal release until higher temperatures were reached.[41] These findings are aligned with the prior research using chitosan-modified agricultural biochar for heavy metal removal.[37]

3.1.4. Crystallinity Study. Powdered samples of pristine and metal-loaded PGB−CS were used for X-ray diffraction studies. The analysis was performed using a Rigaku ULTIMA-IV diffractometer with Cu−Kα radiation (λ = 1.5406 Å), operating at 40 kV and 30 mA. Data were collected over a 2Θ range of 5°−90° at a scanning rate of 10°/min to determine the crystallinity and phase characteristics. XRD graphs of PGB−CS before and after heavy metal adsorption are depicted in Figure S2. The peaks observed for PGB−CS indicated a higher crystallinity (58.96%), which were attributed to the intramolecular hydrogen-bonding interactions within the PGB−CS backbone.[37] Following exposure to metals, the degree of crystallinity was decreased to 49.89%, 44.14%, and 40.51% for Zn^{2+}, Ni^{2+}, and Cu^{2+}, respectively. The degree of crystallinity followed the sequence Cu^{2+} < Ni^{2+} < Zn^{2+}, suggesting that copper exhibited a more favorable layer adsorption compared to nickel and zinc.[12] This order reflects the different affinities of these metals for the PGB−CS composite. The appearance of copper hydroxychloride (peak at 25.28°), nickel nitrate hydroxide (peak at 26.90°), and zinc hydroxychloride (peak at 44.90°) after the adsorption of Cu^{2+}, Ni^{2+}, and Zn^{2+}, respectively, suggested that the metal ions were also adsorbed through surface precipitation, forming sparingly soluble hydroxide phases.[22,31] Comparative scrutiny of postadsorption XRD spectra against the pristine state of PGB−CS shows a smoother spectrum and reduced intensity, suggesting the pore filling by the heavy metals.[39]

3.1.5. FTIR Spectra. For FTIR analysis, fine-ground samples were mixed with KBr in a 1:100 ratio and pressed into transparent pellets using a hydraulic press. The spectra were recorded using a Jasco FTIR-4200 spectrometer in the range of 4000−400 cm^{-1}. The resulting spectra were used to identify the surface functional groups and their changes after metal adsorption. FTIR analysis was conducted for pristine PGB−CS, PGB−CS−Cu^{2+}, PGB−CS−Ni^{2+}, and PGB−CS−Zn^{2+} as shown in Figure 4a−d. The peaks falling within the range of 3900−3450 cm^{-1} signified the vibrations of hydroxyl (−OH) groups. However, post metal adsorption, alterations in peak intensity (3850−3387 cm^{-1}) suggested the surface complexation between metal ions and hydroxyl groups.[42] Simultaneously, peaks from 3400 to 3050 cm^{-1} correspond to the amine ($-NH_2$) groups, showing a smoother profile after adsorption due to electrostatic attraction between them.[31] The presence of C═C in the 2450−1950 cm^{-1} range, with their intensity shifting to 2411−1906 cm^{-1} after metal adsorption, corresponded to an electrostatic attraction.[31] Similarly, the C═O related to the −COOH group, observed in the 1625−1460 cm^{-1} range for PGB−CS, exhibited a shift in intensity (1605−1415 cm^{-1}) post metal adsorption, corresponding to the surface complexation.[43] A peak at 2966.95 cm^{-1}, corresponding to the C−H, observed alterations in intensity after Cu^{2+} adsorption (2973.10 cm^{-1}), indicating hydrogen bonding between them.[12] Furthermore, another peak at 952.05 cm^{-1}, associated with the C−H bonds, displayed a peak alteration (947.94−949.98 cm^{-1}) after adsorption, suggesting changes in the bonding environment.[2] The peaks between 1000 and 1200 cm^{-1} were characteristic of the P−O stretching vibrations, which is indicative of phosphorus−oxygen interactions within the material.[31] Notably, the peak at 1170 cm^{-1} was attributed to the C−O−P stretching, confirming the successful incorporation of phosphorus into the biochar matrix.[22] Furthermore, the possibility of ion exchange between metal ions and native cations present in the PGB−CS composite was supported by quantitative AAS analysis. As shown in Table S3, notable increases in the concentrations of Mg^{2+}, Ca^{2+}, Na^{+}, and K^{+} were observed in the solution after the adsorption of Cu^{2+}, Ni^{2+}, and Zn^{2+}. The release of these cations indicated that they were displaced by the incoming metal ions during the adsorption process, confirming ion exchange as one

https://doi.org/10.1021/acsomega.5c04698
ACS Omega XXXX, XXX, XXX−XXX

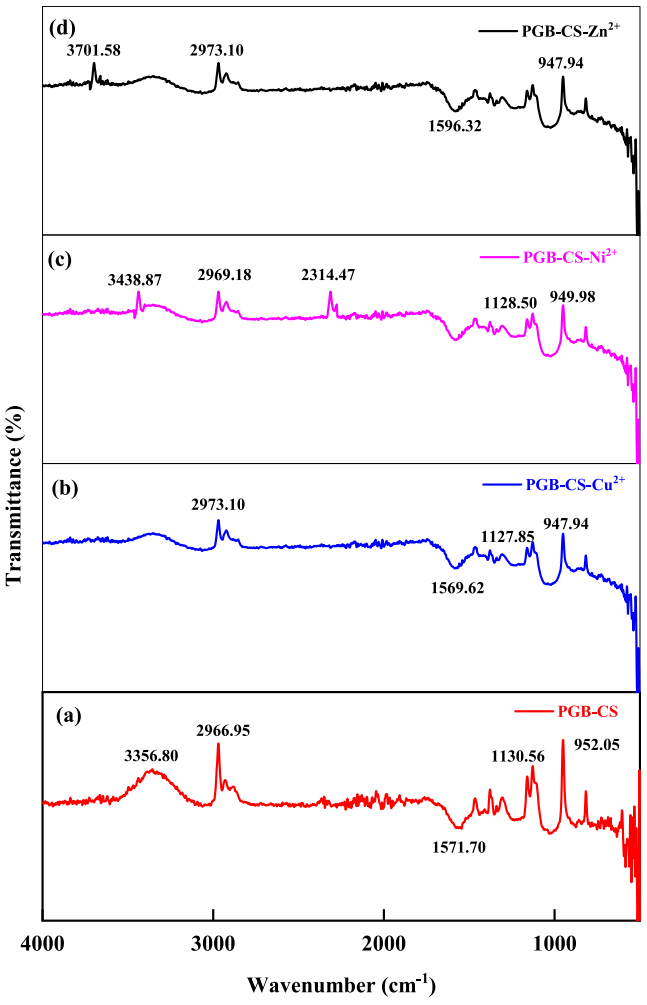

Figure 4. FTIR study: (a) pristine PGB−CS; (b) PGB−CS−Cu^{2+} after adsorption; (c) PGB−CS−Ni^{2+} after adsorption; and (d) PGB−CS−Zn^{2+} after adsorption.

of the active mechanisms. This conclusion was further supported by subtle FTIR peak shifts in the 1000−1200 cm^{-1} region, corresponding to the P−O and C−O−P vibrations. These groups were involved in ion coordination, and the observed shifts suggested an altered bonding environment postadsorption, consistent with ion-exchange interactions.[22,39]

3.1.6. XPS Analysis. X-ray photoelectron spectroscopy was carried out by using a Thermo Fisher Scientific K-α instrument equipped with a monochromatic X-ray source (1486.6 eV). Samples were fixed on a double-sided carbon tape and introduced into the analysis chamber under ultrahigh vacuum conditions. Survey and high-resolution scans were obtained for key elements, and charge compensation was applied by using a low-energy electron flood gun to prevent sample charging. The overall XPS spectra of pristine PGB−CS and after metal ion adsorption are presented in Figure 5a−d. In the C 1s spectrum, two distinct peaks were observed at 284.88 and 288.78 eV, agreeing with C−C/C═C and C═O, respectively (Figure 5e). After adsorption, these peaks shifted to 284.10 and 288.08 eV after Cu^{2+} adsorption (Figure S3a), 284.48 and 288.38 eV after Ni^{2+} adsorption (Figure S3b), and 284.68 and 288.49 eV after Zn^{2+} adsorption (Figure S3c). Additionally, a peak at 285.39 eV, attributed to the complex ($(-CH_3COO)_2 \cdot 2H_2O-$), was detected following metal adsorption.[40] In the O 1s spectrum before adsorption (Figure 5f), two peaks were noted: peak 1 at 531.9 eV, related to O−H, and peak 2 at 532.5 eV, related to C−O. Postadsorption, these peaks shifted to 530.06 and 531.29 eV after Cu^{2+} adsorption (Figure S3d), 531.09 and 531.81 eV after Ni^{2+} adsorption (Figure S3e), and 531.54 and 532.14 eV after Zn^{2+} adsorption (Figure S3f). An additional peak at 535.52 eV, associated with the complex (CH_3CH_2COOH), was observed after metal adsorption. This suggested that carboxylic and hydroxyl groups were involved in metal adsorption through ion exchange.[44] The N 1s spectrum revealed two main peaks before adsorption (Figure 5g): peak 1 at 399.08 eV, corresponding to $-NH-/-NH_2$, and peak 2 at 406.98 eV, corresponding to $-NH_2-/-NH_3$. After metal adsorption, these peaks shifted to 398.12 and 406.01 eV for Cu^{2+} adsorption (Figure S3g), 398.47 and 406.31 eV for Ni^{2+} adsorption (Figure S3h), and 398.81 and 406.58 eV for Zn^{2+} adsorption (Figure S3i). A peak at 404.78 eV, attributed to C−N, was identified following metal adsorption. These observations indicated that the amine groups acted for metal binding.[45] The distinct peaks for Cu 2p (932.9, 952.77, and 962.38 eV), Ni 2p (855.42, 869.5, 850.9, and 847.5 eV), and Zn 2p (1021.86, 1044.95, and 1047.95 eV) spectra are attributed to the metal binding with carbon, oxygen, and nitrogen elements, confirming the successful adsorption of metal ions on the PGB−CS surface (Figure 5h−j). Similarly, for the P 2p spectrum, three distinct peaks were observed at 133.311, 134.796, and 139.377 eV corresponding to phosphate (PO_4^{3-}) and phosphite ($-PO_3^{3-}$) groups (Figure 5k).

3.2. Three Levels of Optimization. *3.2.1. First Level of Optimization: Pyrolysis Temperature and Pyrolysis Time.* The pyrolysis temperature has a major impact on the adsorption performance of GB. In this study, q_e was evaluated at pyrolysis temperatures (500−600 °C) for a metal concentration of 1000 mg/L and an adsorbent dosage of 1 g/L, as presented in Figure 6a. For Cu^{2+} adsorption, q_e increased by 13.74% (107.21 mg/g at 500 °C to 121.94 mg/g at 550 °C). However, at 600 °C, the increase was only 4.84%, with q_e increased to 127.85 mg/g. Similar trends were also observed for Ni^{2+} and Zn^{2+} adsorption. To validate the experimental results, EDX analysis of biochar (GB) was performed at all pyrolysis temperatures and is presented in Table S4. The results revealed that carbon content increased by 12.67% between 500 and 550 °C and changed by only 3.54% from 550 to 600 °C. Surface area analysis as described in Section 3.1.1 further validated these findings, showing alterations in pore diameter and surface area at different pyrolysis temperature ranges. Balancing energy requirements with product performance led to the selection of a pyrolysis temperature of 550 °C for further studies. Similar observations have been reported in a study involving the removal of heavy metals using a phosphorus-engineered poplar sawdust biochar.[46] Further, the impact of pyrolysis time on metal removal was studied and the results are presented in Figure 6b. For Cu^{2+}, q_e increased by 20.30% when the pyrolysis time was increased from 1 to 2 h; however, it increased by only 5.10% when the pyrolysis time was extended from 2 to 3 h. Similar trends were observed for Ni^{2+} and Zn^{2+} adsorption. These results suggested that extending the pyrolysis time beyond 2 h did not significantly enhance the adsorption capacity of GB and considered it as an optimum condition. A similar trend for the effect of pyrolysis time has been reported in metal removal using NaOH-modified fly ash.[47]

https://doi.org/10.1021/acsomega.5c04698
ACS Omega XXXX, XXX, XXX−XXX

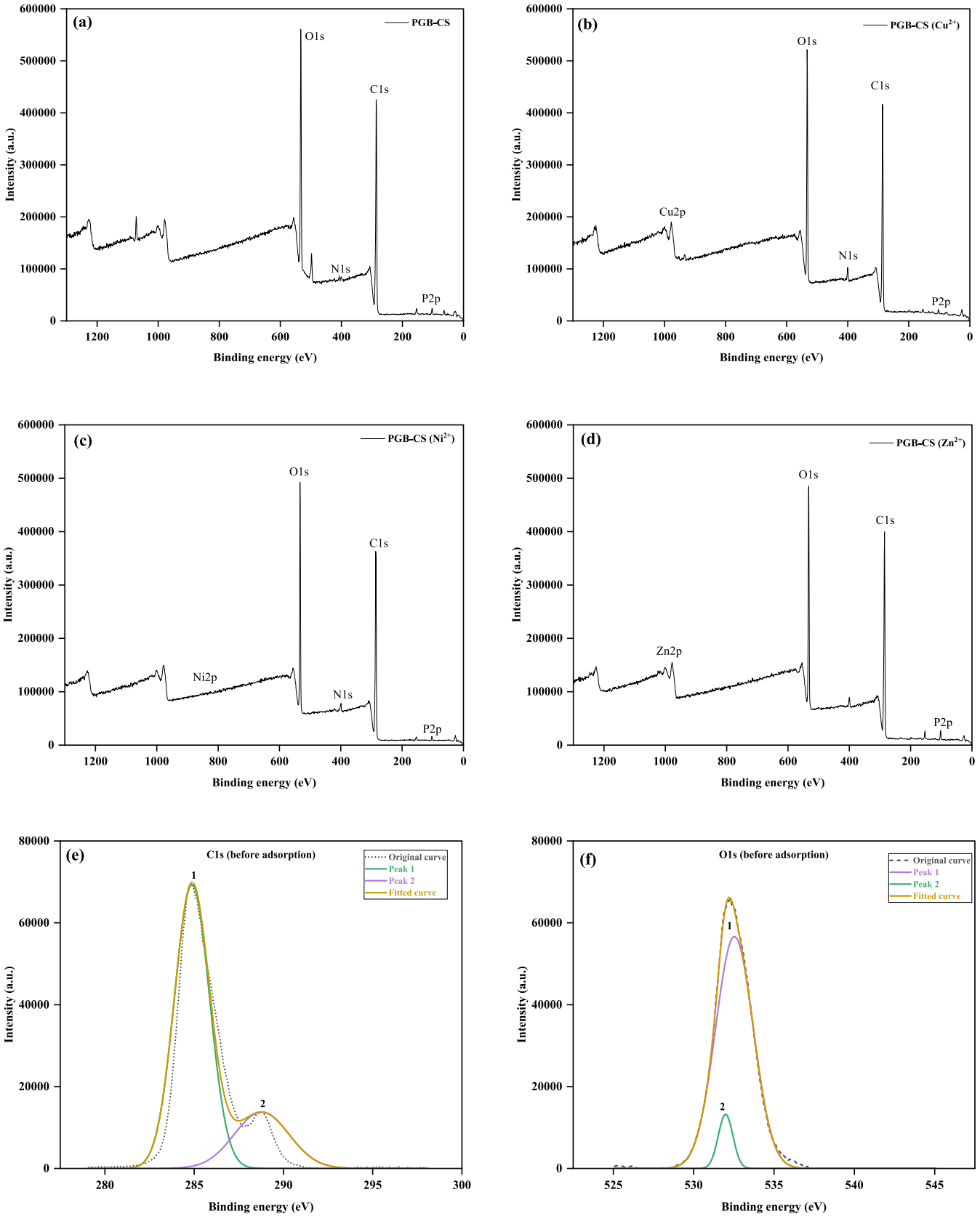

Figure 5. continued

https://doi.org/10.1021/acsomega.5c04698
ACS Omega XXXX, XXX, XXX−XXX

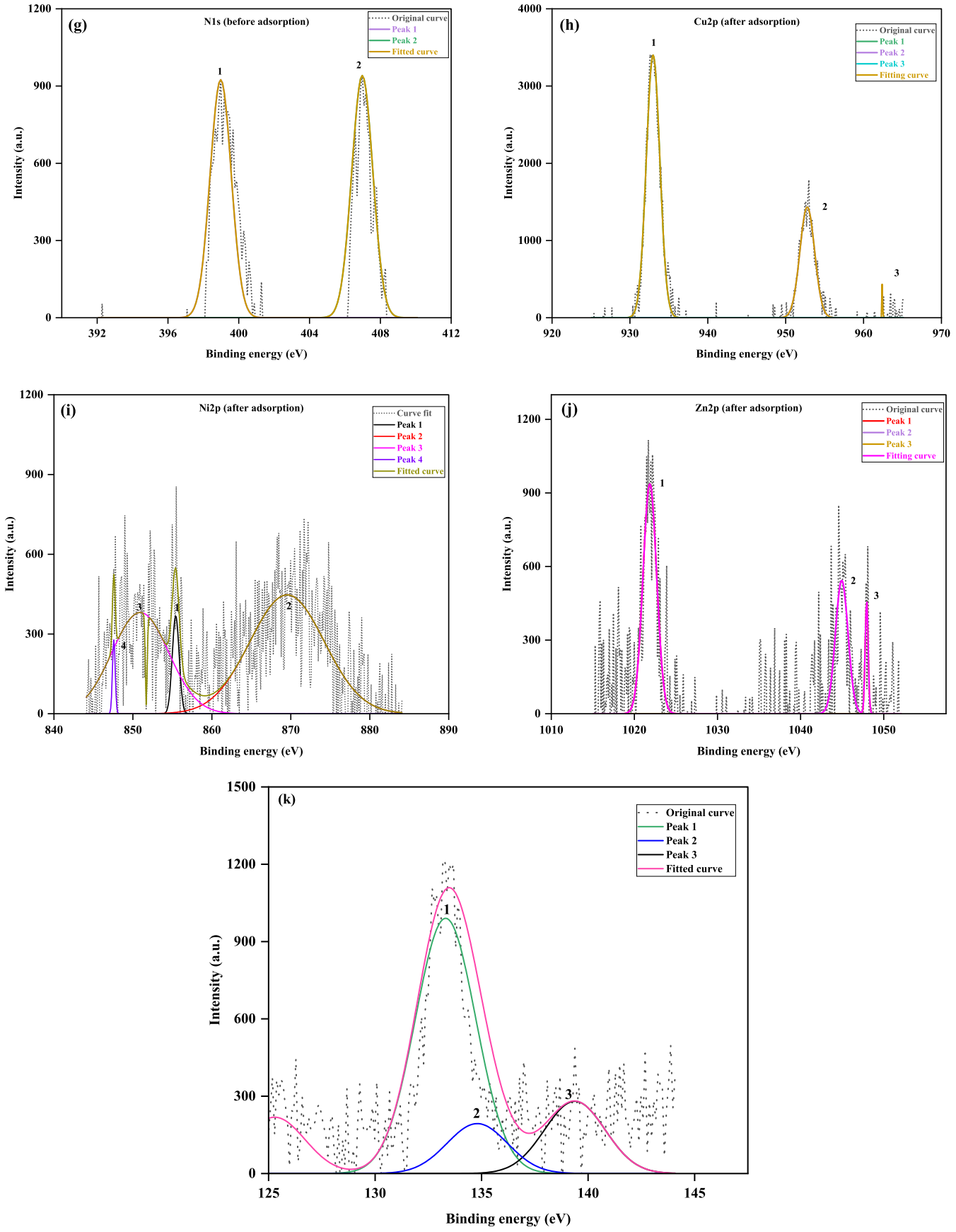

Figure 5. XPS results: (a) survey view of PGB−CS; (b) survey view of PGB−CS (Cu^{2+}); (c) survey view of PGB−CS (Ni^{2+}); (d) survey view of PGB−CS (Zn^{2+}); (e) C 1s (before adsorption); (f) O 1s (before adsorption); (g) N 1s (before adsorption); (h) Cu 2p (after Cu^{2+} adsorption); (i) Ni 2p (after Ni^{2+} adsorption); (j) Zn 2p (after Zn^{2+} adsorption); and (k) P 2p (before adsorption).

https://doi.org/10.1021/acsomega.5c04698
ACS Omega XXXX, XXX, XXX−XXX

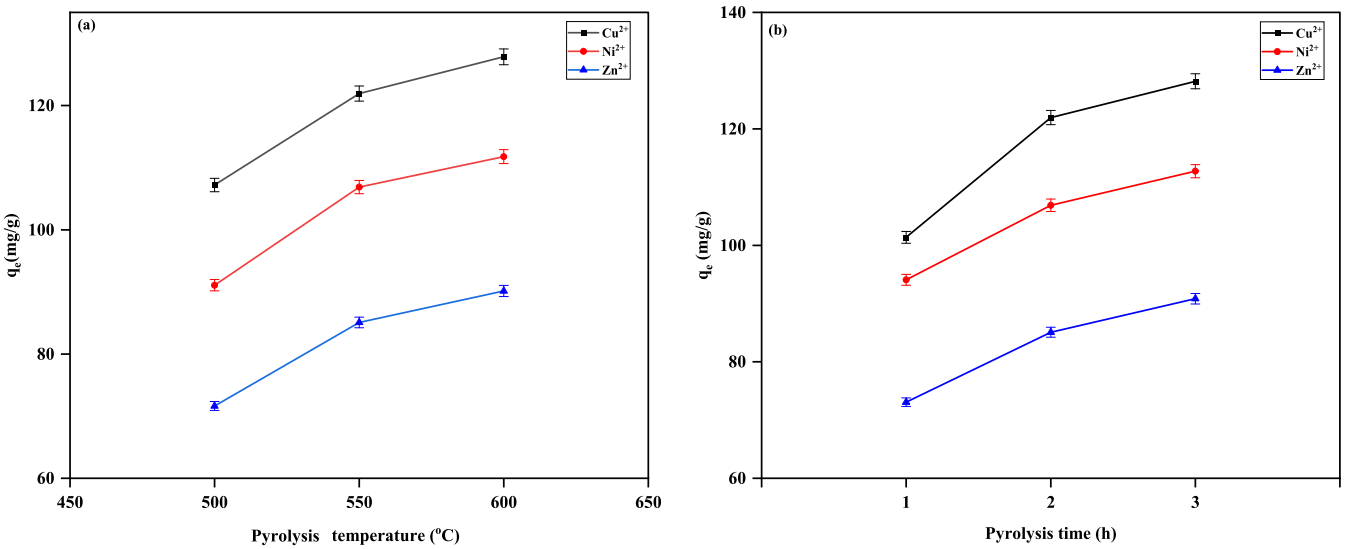

Figure 6. First level of process optimization: (a) pyrolysis temperature and (b) pyrolysis time.

Table 2. RSM Results

run	A: time (min)	B: dosage (g/L)	C: metal concentration (mg/L)	response (R_1): q_e (Cu^{2+}), mg/g	response (R_2) q_e (Ni^{2+}), mg/g	response (R_3): q_e (Zn^{2+}), mg/g
1	20	1	550	201.48	167.18	121.71
2	100	1	100	207.18	155.84	108.43
3	100	1	1000	245.87	192.73	141.81
4	180	1	550	234.95	185.16	135.17
5	20	5.5	100	158.76	122.1	73.47
6	20	5.5	1000	175.18	139.17	84.76
7	100	5.5	550	190.23	151.78	97.6
8	100	5.5	550	192.49	156.1	103.8
9	100	5.5	550	196.17	153.61	99.19
10	100	5.5	550	199.42	146.94	94.13
11	100	5.5	550	203.14	149.7	96.07
12	180	5.5	100	177.43	137.14	83.98
13	180	5.5	1000	190.18	157.13	101.32
14	20	10	550	170.93	134.19	74.97
15	100	10	100	175.34	133.94	71.94
16	100	10	1000	201.36	147.64	84.38
17	180	10	550	195.71	145.91	92.8
18	36.00	1	1000	210.12	-	-
19	36.00	1	1000	213.94	-	-
20	36.00	1	1000	205.17	-	-
21	20	1	1000	-	161.24	-
22	20	1	1000	-	165.19	-
23	20	1	1000	-	169.76	-
24	20	1	1000	-	-	112.94
25	20	1	1000	-	-	115.73
26	20	1	1000	-	-	121.48

To further support the selection of 550 °C as the optimal pyrolysis temperature, the activation energy (E_a) was estimated using the Coats−Redfern method. The Coats−Redfern equation for a first-order decomposition reaction is given in eq 4

$$\ln\left(\frac{-\ln(1-\alpha)}{T^2}\right) = \ln\left(\frac{AR}{\beta E_a}\right) - \left(\frac{E_a}{RT}\right) \quad (4)$$

where α is the fractional weight loss, T is the absolute temperature (K), β is the heating rate (15 °C/min), R is the universal gas constant (8.314 J/mol·K), A is the pre-exponential factor, and E_a is the activation energy (kJ/mol). The activation energies at selected pyrolysis temperatures were determined to be 0.50 kJ/mol (400 °C), 0.78 kJ/mol (500 °C), 1.23 kJ/mol (550 °C), and 4.94 kJ/mol (600 °C). The moderate activation energy at 550 °C indicated that the decomposition and carbonization process were thermally efficient. In contrast, the sharp increase in activation energy at 600 °C suggested a higher energy demand, despite only marginal improvements in structural properties such as surface area and pore diameter (Section 3.1.1) and carbon content (Section 3.1.2). Furthermore, the relatively small increase in

https://doi.org/10.1021/acsomega.5c04698
ACS Omega XXXX, XXX, XXX−XXX

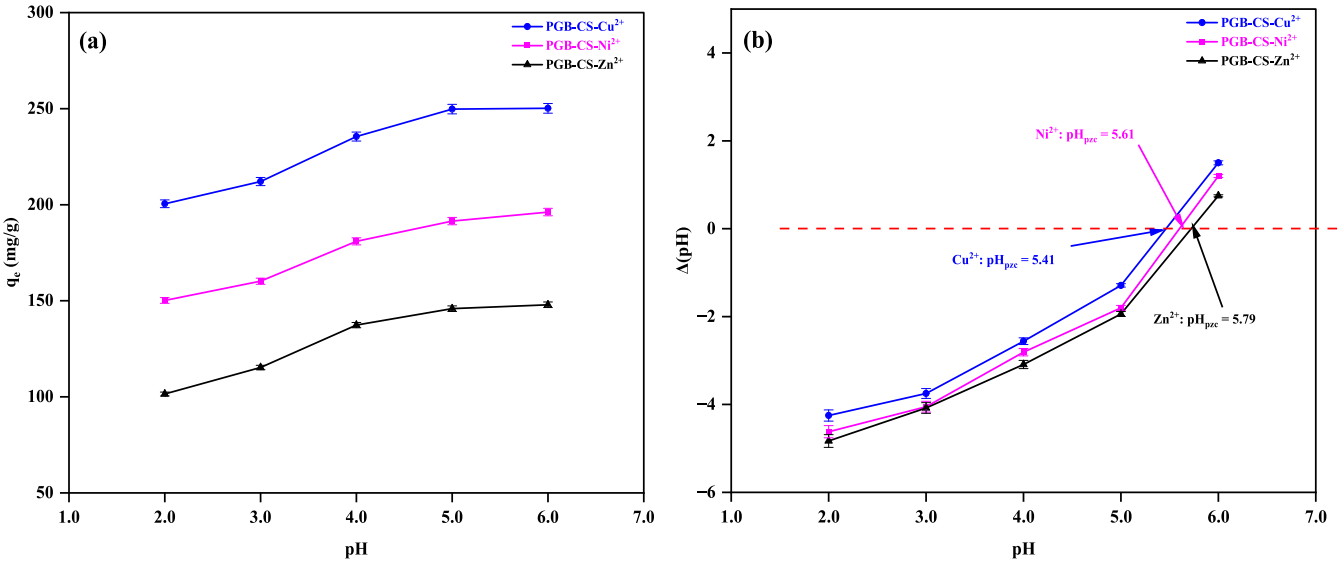

Figure 7. (a) pH study; (b) pH_{pzc} determination for Cu^{2+}, Ni^{2+}, and Zn^{2+}.

the adsorption capacity at 600 °C supported the idea that 550 °C represented an optimal balance between enhanced adsorption performance and energy efficiency. These combined observations justified the selection of 550 °C as the optimal pyrolysis temperature for further studies.

3.2.2. Second Level of Optimization: RSM Study. The optimization of three critical variables, batch time (A), adsorbent dosage (B), and metal concentration (C) to maximize q_e, was conducted using RSM. The RSM results for 17 runs are given in Table 2.

The factor−response dynamics for three metal ions, Cu^{2+}, Ni^{2+}, and Zn^{2+}, in a quadratic form given by eqs 5, 6, and 7, respectively

$$Cu^{2+}: q_e = 196.29 + 11.49A - 18.27B + 11.74C - 2.17AB - 0.91AC - 3.17BC - 13.79A^2 + 18.26B^2 - 7.12C^2;\ R_1^2 = 0.97 \quad (5)$$

$$Ni^{2+}: q_e = 151.63 + 7.84A - 17.40B + 10.96C - 1.57AB + 0.73AC - 5.80BC - 6.08A^2 + 12.57B^2 - 6.66C^2;\ R_2^2 = 0.98 \quad (6)$$

$$Zn^{2+}: q_e = 98.16 + 7.30A - 22.88B + 9.31C + 1.09AB + 1.51AC - 5.23BC - 3.88A^2 + 11.88B^2 - 8.40C^2;\ R_3^2 = 0.98 \quad (7)$$

The coefficient of regression (R^2) was obtained close to 1.0 for all three metals, demonstrating a minimal deviation and high predictive accuracy of the models. Graphical representations of predicted Vs residuals q_e and actual Vs predicted q_e for three metals are presented in Figures S4 and S5, respectively. Further, the interplay between binary factors on q_e for Cu^{2+}, Ni^{2+}, and Zn^{2+} is illustrated in Figures S6−S8, respectively. The normal probability plots of residuals for Cu^{2+}, Ni^{2+}, and Zn^{2+} are shown in Figure S9. The lack-of-fit test results, including F-values and p-values for all three metal ions, are presented in Table S5. The p-values for the lack-of-fit tests (0.3605 for Cu^{2+}, 0.5657 for Ni^{2+}, and 0.8183 for Zn^{2+}) were all greater than 0.05, indicating that the quadratic models provided an adequate fit for all three metal ions.[31,39] Furthermore, the normal probability plots (Figure S9) showed that the residuals for all three metal ions aligned closely along the straight reference line, suggesting that the residuals were approximately normally distributed, with no strong skewness.[48] These results collectively confirmed that the quadratic models were appropriate for accurately describing the adsorption behavior of Cu^{2+}, Ni^{2+}, and Zn^{2+} under the tested conditions.

The q_e values determined using RSM were 221.56 mg/g for Cu^{2+}, 175.47 mg/g for Ni^{2+}, and 127.46 mg/g for Zn^{2+}. These values were obtained under optimal conditions of 1000 mg/L, 36 min, and 1 g/L for Cu^{2+}, and 20 min, 1000 mg/L, and 1 g/L for both Ni^{2+} and Zn^{2+}, respectively. To validate these optimal conditions, experiments were repeated three times at the determined optimal settings (runs 18−20 for Cu^{2+}, runs 21−23 for Ni^{2+}, and runs 24−26 for Zn^{2+}) as presented in Table 2. An error analysis was conducted for the repeated experiments and is exhibited in Table S6. Furthermore, the effect of contact time, initial metal ion concentration, and adsorbent dosage on the removal efficiency of Cu^{2+}, Ni^{2+}, and Zn^{2+} was studied and is illustrated in Figure S10a−c. The longer equilibrium contact time for Cu^{2+} (50 min) compared with that of Ni^{2+} (20 min) and Zn^{2+} (20 min) reflected a slower diffusion, potentially due to stronger electrostatic interactions with the adsorbent.[22] A similar difference in the equilibrium time was reported in a previous study using phosphoric acid-modified bentonite−chitosan composite beads for the removal of Cu^{2+}, Ni^{2+}, and Zn^{2+}.[22] Notably, the parametric trends and optimum values identified in this study were in close agreement with those obtained through RSM-based statistical analysis, further validating the robustness and predictive accuracy of the developed models.

3.2.3. Third Level of Optimization: pH Study. The pH of the industrial effluent changes significantly periodically, which motivated us to study the pH effect on adsorbent performance.[49] This study examined the effect of pH (2.0−6.0) at constant optimum conditions determined by the RSM study, and the results are depicted in Figure 7a. At low pH, the presence of H^+ ions competes with the adsorbent on the adsorbent surface, leading to electrostatic repulsion and thus

https://doi.org/10.1021/acsomega.5c04698
ACS Omega XXXX, XXX, XXX−XXX

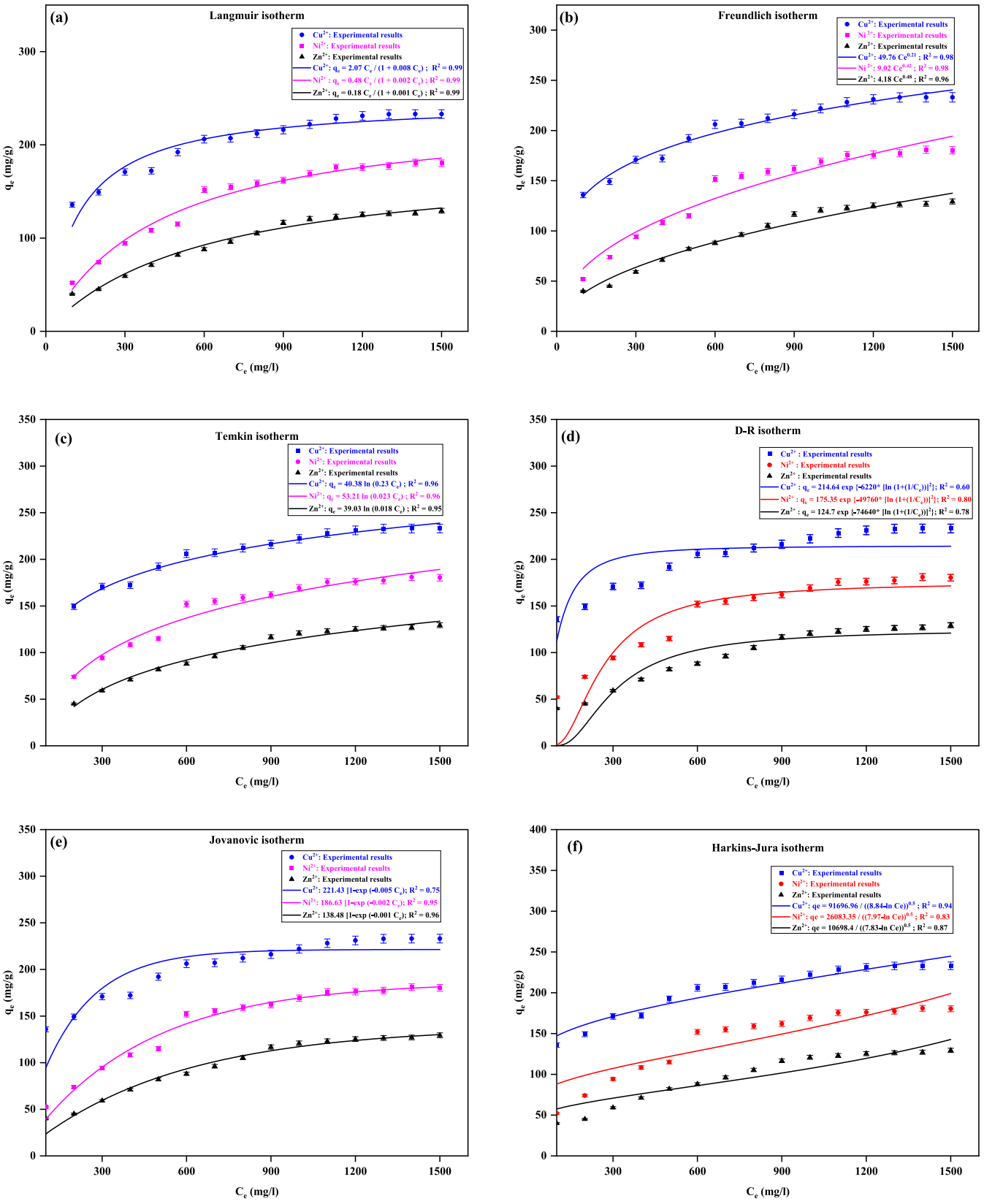

Figure 8. Isotherm study results: (a) Langmuir, (b) Freundlich, (c) Temkin, (d) D−R, (e) Jovanovic, and (f) Harkins−Jura.

reducing the adsorption performance.[2] As pH increases, the H^+ ion presence diminishes, enhancing the adsorption capacity for heavy metals. The metal hydroxide precipitation was witnessed at pH 6.0 and above, which was attributed to the decreased solubility of metal hydroxides at high pH or formation of complex ions in wastewater, which precipitated at high pH.[31] The PGB−CS adsorbent proved optimal performance at pH 5.0 and obtained q_e as 249.78 mg/g for Cu^{2+}, 191.48 mg/g for

https://doi.org/10.1021/acsomega.5c04698
ACS Omega XXXX, XXX, XXX−XXX

Table 3. Isotherm Model Fitting Results for Cu^{2+}, Ni^{2+}, and Zn^{2+}

isotherm model	parameters	Cu^{2+}	Ni^{2+}	Zn^{2+}
Langmuir	q_m (mg/g)	247.49	239.46	185.2
	K_L (L/mg)	0.008	0.002	0.001
	R_L	0.60	0.55	0.51
	R^2	0.99	0.99	0.99
Freundlich	K_F (L/g)	49.76	9.02	4.18
	n (unitless)	4.64	2.38	2.09
	R^2	0.98	0.96	0.96
Temkin	K_T (L/g)	0.23	0.023	0.018
	b_T (J/mol)	61.35	46.56	63.48
	R^2	0.96	0.96	0.95
D−R	q_m (mg/g)	214.64	175.35	124.7
	β (mol^2 kJ^{-2})	0.001	9.45×10^{-4}	8.58×10^{-4}
	E_a (kJ/mol)	22.36	23.01	24.14
	R^2	0.60	0.80	0.78
Jovanovic	q_m (mg/g)	221.43	186.63	138.48
	K_j (L/mg)	−0.005	−0.0023	−0.0018
	R^2	0.75	0.95	0.96
Harkins−Jura	A_{HJ}	91,696.96	26,083.35	10,698.4
	B_{HJ}	8.84	7.97	7.83
	R^2	0.94	0.83	0.87

Table 4. Comparison of q_m by Langmuir Isotherm for the Removal of Heavy Metals

adsorbent	solution pH	equilibrium time (min)	adsorbent properties	q_m (mg/g)	metal	refs
tetraethylenepentamine-modified chitosan/$CoFe_2O_4$ composite	5.0	50	pore dia.: 121 nm	168.06	Cu^{2+}	55
$KMnO_4$-modified walnut shell biochar	5.0	360	surface area: 333.19 m^2/g, pore volume: 0.16 cm^3/g, pore dia.: 1.95 nm	30.18	Cu^{2+}	44
PGB−CS	5.0	90	surface area: 167.98 m^2/g; pore volume: 0.189 cm^3/g; pore dia.: 9.18 nm	247.49	Cu^{2+}	this study
chitosan−polyvinyl alcohol membrane	6.0	300	surface area: 0.7 m^2/g	75.5	Ni^{2+}	56
cross-linked chitosan hydrogels	6.0	180	-	78.0	Ni^{2+}	53
PGB−CS	5.0	90	surface area: 167.98 m^2/g; pore volume: 0.189 cm^3/g; pore dia.: 9.18 nm	239.46	Ni^{2+}	this study
CS/clay/biochar composite	5.0	540	surface area: 272.49 m^2/g, pore diameter: 1.9842 nm, pore volume: 0.1352 cm^3/g	134.6	Zn^{2+}	54
$FeCl_3$-modified cotton husk−chitosan composite	5.0	250	pore dia.: 9.37 nm, pore volume: 0.175 cm^3/g, surface area: 127.89 m^2/g	117.50	Zn^{2+}	21
$KMnO_4$-modified walnut shell biochar	5.0	360	surface area: 333.19 m^2/g, pore volume: 0.16 cm^3/g, pore dia.: 1.95 nm	58.96	Zn^{2+}	44
PGB−CS	5.0	90	surface area: 167.98 m^2/g; pore volume: 0.189 cm^3/g; pore dia.: 9.18 nm	185.20	Zn^{2+}	this study

Ni^{2+}, and 145.91 mg/g for Zn^{2+} under optimal parameters determined through the RSM study. The pH study was further validated by determining pH_{pzc}, and the results are shown in Figure 7b. The pH_{pzc} values were determined as 5.41, 5.61, and 5.79 for Cu^{2+}, Ni^{2+}, and Zn^{2+}, respectively. Below the pH_{pzc}, q_e was decreased due to the increasing presence of H^+ ions in the solution, which repels the adsorption of metals on the PGB−CS surface. The adsorption operated below pH_{pzc} generally resulted in a positively charged surface, which did not have a favored cationic metal adsorption purely through electrostatic attraction. However, effective adsorption still occurred at pH 5.0 due to the involvement of additional mechanisms, including surface complexation and coordination with functional groups (−OH and $-NH_2$) on the adsorbent. Moreover, as the pH increased beyond 5.0, metal hydroxide precipitation was observed (at pH 6.0 and above), which interfered with true adsorption and limited the selection of higher pH values. Hence, pH 5.0 represented a balance point for minimizing H^+ competition, avoiding precipitation, and enabling high adsorption through both electrostatic and nonelectrostatic interactions. The influence of pH on heavy metal removal observed in this study aligned with the findings from previous studies that utilized modified adsorbents like poly(vinyl alcohol)-modified chitosan and phosphoric acid-modified bentonite−chitosan composite beads.[22,31]

3.3. Isotherm, Kinetic, and Thermodynamic Studies.

3.3.1. Isotherm Study. The isotherm study was conducted using six nonlinear models as listed in Table 1, within a metal concentration range of 100−1500 mg/L under the operating conditions as determined by RSM: 1 g/L and 36 min for Cu^{2+}, 1 g/L and 20 min for Ni^{2+}, and 1 g/L and 20 min for Zn^{2+}. The curve fittings from the isotherm study are depicted in Figure 8a−f, with the calculated isotherm parameters and R^2 values listed in Table 3. The analysis showed that the Freundlich, Temkin, and Langmuir isotherms exhibited higher R^2 values compared to the D−R, Jovanovic, and Harkins−Jura isotherms for all three metal ions. The Langmuir isotherm, with an R^2 value close to 1.0, suggested a good fit with the experimental

https://doi.org/10.1021/acsomega.5c04698
ACS Omega XXXX, XXX, XXX−XXX

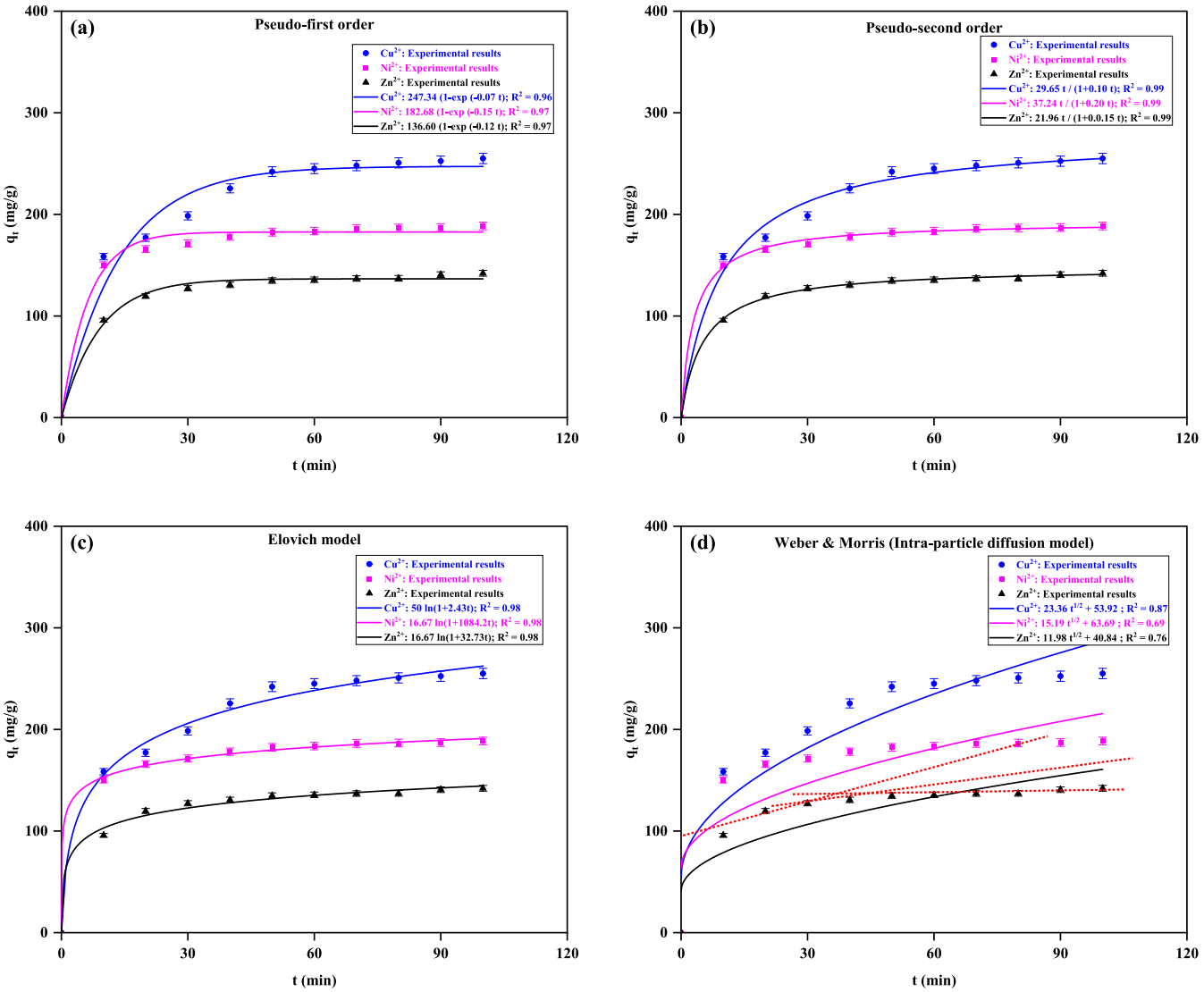

Figure 9. Kinetic model fitting results: (a) pseudo-first-order, (b) pseudo-second-order, (c) Elovich, and (d) Weber and Morris IPD models.

results, indicating that monolayer adsorption of heavy metals occurred on the surface of PGB−CS.[50] The constant of the Freundlich isotherm ($1/n$) and separation factor (R_L) in the Langmuir isotherm obtained less than 1.0 for all metal ions, suggesting that the favorable and spontaneous adsorption occurred on the surface of PGB−CS.[31] The dominance of the Langmuir-type adsorption suggested that metal ions were adsorbed with the monolayer formation.[51] This behavior was attributed to strong interactions between the metal ions and functional groups (−OH, $-NH_2$, −COOH, and $-PO_4^{3-}$) presented on the PGB−CS surface, which facilitated localized chemisorptive binding. Although the Freundlich model also showed a reasonable fit with respect to R^2 values (Cu^{2+}: 0.98, Ni^{2+}: 0.96, Zn^{2+}: 0.96), implying some degree of surface heterogeneity and possible multilayer adsorption; however, the high R^2 values for the Langmuir model (Cu^{2+}: 0.99, Ni^{2+}: 0.99, Zn^{2+}: 0.99) indicated that monolayer adsorption was the dominant mechanism compared to heterogeneous. The q_m predicted by the Langmuir isotherm resulted in 247.49 mg/g for Cu^{2+}, 239.46 mg/g for Ni^{2+}, and 185.2 mg/g for Zn^{2+}, possessing the capability of PGB−CS for eliminating heavy metals. The mean adsorption energy (E_a) in the D−R isotherm designates different adsorption mechanisms.[52] In this study, E_a attained as 22.36 kJ/mol for Cu^{2+}, 23.01 kJ/mol for Ni^{2+}, and 24.14 kJ/mol for Zn^{2+}, suggesting that the adsorption predominantly occurred through chemisorption compared to physisorption.[37] The comparison of q_m with the reported results for the removal of Cu^{2+}, Ni^{2+}, and Zn^{2+} is provided in Table 4.

The superior performance of the PGB−CS composite compared with other reported adsorbents was attributed to its unique combination of chemical functionality and structural properties. The phosphoric acid treatment of biochar introduced phosphate-based functional groups and enhanced the surface area (102.98−167.98 m^2/g) and pore diameter (7.56−9.18 nm) of the adsorbent. These features facilitated stronger electrostatic interactions and surface complexation with the heavy metals. Chitosan, rich in amine and hydroxyl groups, contributed significantly to metal ion coordination through chelation. The integration of chitosan onto the porous and phosphate-rich biochar created a hybrid structure with high binding sites and bonding through chemisorption. In contrast, materials such as $KMnO_4$-modified walnut shell biochar possessed oxidized surfaces but lacked strong chelating

https://doi.org/10.1021/acsomega.5c04698
ACS Omega XXXX, XXX, XXX−XXX

functionalities, which limited their binding strength and selectivity toward heavy metals.[44] Similarly, chitosan-based hydrogels and membranes, while rich in amine groups, often suffered from slow diffusion due to swelling and weaker mechanical integrity.[53] Adsorbents such as $FeCl_3$-modified cotton husk−chitosan composites or cross-linked chitosan hydrogels lacked the pore interconnectivity, which contributed to slower adsorption kinetics and reduced uptake capacity.[21] Furthermore, the PGB−CS composite offered a more homogeneous distribution of chitosan on the biochar surface compared to CS/clay/biochar blends, where phase separation or poor interaction between components reduced the number of active sites available.[54] The combination of chemical affinity, tailored surface functionality, and a physically robust framework distinguished PGB−CS as a more efficient and practical adsorbent for multimetal removal.

While the isotherm models applied in this study provided meaningful insight into the adsorption behavior of the PGB−CS adsorbent, certain limitations were identified in their applicability. The Langmuir model, which showed the best correlation with the experimental data, assumed monolayer adsorption, which may not have fully represented the porous surface characteristics of the PGB−CS material. The Freundlich and Temkin models, although they offered reasonable fits, were empirical in nature and did not account for the saturation of the adsorption sites or the possibility of site interactions on the complex surface of the composite. Additionally, the Dubinin−Radushkevich and Harkins−Jura models relied on idealized assumptions regarding energy distribution and multilayer adsorption, which may not have aligned with the actual surface energetics of PGB−CS. These limitations indicated that while the models were effective in describing equilibrium behavior under controlled conditions, their predictive capability for real and dynamic systems, such as multimetal industrial effluents, was constrained.

3.3.2. Kinetic Study. The kinetic study utilized four nonlinear models (pseudo-first-order, pseudo-second-order, Elovich, and Weber and Morris intraparticle diffusion) as detailed in Table 1, with graphical fitting results shown in Figure 9 and model parameters, including R^2 values, listed in Table 5. The PFO and PSO models were usually used to represent physisorption- and chemisorption-based kinetics, respectively.[57] The Elovich model is typically applied to systems with heterogeneous surface energies,[58] whereas Weber and Morris's IPD model is commonly employed to evaluate the contribution of intraparticle diffusion as a potential rate-limiting step during adsorption.[59] These kinetic models were frequently reported in the literature for the heavy metal removal from wastewater using adsorbents such as MnO_x-modified cocopeat biocar,[13] zwitterion−chitosan bed,[60] poly(vinyl alcohol)-modified chitosan,[31] hydroxyapatite−chitosan composite,[61] coal fly ash−chitosan composite,[39] and chitosan−magnetic biochar composite.[21]

Table 5. Kinetic Model Fitting Results for Cu^{2+}, Ni^{2+}, and Zn^{2+}

kinetic model	parameters	Cu^{2+}	Ni^{2+}	Zn^{2+}
Pseudo-first order	q_e (mg/g)	247.34	182.68	136.60
	K_1 (min^{-1})	0.07	0.15	0.12
	R^2	0.96	0.97	0.97
Pseudo-second order	q_e (mg/g)	278.97	192.96	148.2
	K_2 (g mg^{-1} min^{-1})	3.81×10^{-4}	0.001	0.001
	h (mg g^{-1} min^{-1})	29.65	37.24	21.96
	R^2	0.99	0.99	0.99
Elovich model	α (mg g^{-1} min^{-1})	121.97	18,070.6	545.6
	β (min^{-1})	0.02	0.06	0.06
	R^2	0.98	0.98	0.98
Weber and Morris	$k_{W\&M}$ (mg/g $min^{-1/2}$)	23.36	15.19	11.98
	C	53.92	63.69	40.84
	R^2	0.87	0.69	0.76

The adsorption capacities for all three metal ions were increased over time and eventually reached a stable equilibrium. The kinetic analysis exhibited two distinct phases: a rapid adsorption phase within the first 36 min for Cu^{2+} and an adsorption phase within 20 min for both Ni^{2+} and Zn^{2+}, followed by a slower adsorption phase approaching equilibrium. This trend was supported by the initial adsorption rates (h) derived from the PSO model, which were 29.65, 37.24, and 21.96 $mg \cdot g^{-1} \cdot min^{-1}$ for Cu^{2+}, Ni^{2+}, and Zn^{2+}, respectively. These relatively high h values indicated a fast adsorption process at the beginning, primarily driven by the abundance of readily accessible active sites and low external mass transfer resistance.[62] The PSO model yielded the highest fit ($R^2 = 0.99$ for all metals), confirming that chemisorption was the dominant mechanism.[63] Notably, the Elovich model also produced a high correlation coefficient ($R^2 = 0.98$), indicating that surface heterogeneity also significantly influenced the adsorption behavior. The initial adsorption rates (α) obtained in the Elovich model were 121.97, 18,070.6, and 545.6 $mg \cdot g^{-1} \cdot min^{-1}$ for Cu^{2+}, Ni^{2+}, and Zn^{2+}, respectively. Although these α values were different from the h values of the PSO model, especially for Ni^{2+}. The higher magnitude of α, particularly for Ni^{2+}, suggested a rapid surface coverage facilitated by a high affinity between metal ions and active sites.[63] This alignment in trends supported the hypothesis that adsorption occurred on a heterogeneous surface, where both chemisorption and energetically diverse active sites were involved in the initial uptake.[64] Similar observations were made in the kinetic studies for heavy metal removal using poly(vinyl alcohol)-modified chitosan,[31] magnetic biochar−chitosan composite,[21] and manganese ferrite nanoparticles.[51]

The intraparticle diffusion (IPD) model showed lower R^2 values (0.87 for Cu^{2+}, 0.69 for Ni^{2+}, and 0.76 for Zn^{2+}), indicating that intraparticle diffusion was not the sole rate-limiting mechanism. The IPD plots revealed three stages: an initial linear portion with a steep slope, reflecting external surface adsorption; a second stage with a reduced slope, attributed to the gradual diffusion into internal pores; and a final plateau phase indicating equilibrium.[65] The nonzero intercept (C) values resulted as 53.92, 63.69, and 40.84 mg/g for Cu^{2+}, Ni^{2+}, and Zn^{2+}, respectively, which reflected a significant contribution from boundary layer effects, particularly in the early adsorption phase.[66] The higher C value for Ni^{2+} implied a strong external mass transfer resistance due to its higher affinity and faster uptake rate. Additionally, the composite structure of PGB−CS included a mesoporous nature restricted diffusion through narrow or tortuous pores, further reducing the significance of IPD as the primary rate-determining step. Although the PSO model provided a good fit to the experimental data, its limitations were acknowledged. The model assumed chemisorption as the sole rate-limiting step but did not account for external mass transfer or

https://doi.org/10.1021/acsomega.5c04698
ACS Omega XXXX, XXX, XXX−XXX

intraparticle diffusion, which were relevant for the porous materials like PGB−CS. The IPD model, despite offering insights into diffusion stages, showed low R^2 values and did not fully capture the overall adsorption process. Surface adsorption and film diffusion likely contributed in parallel, especially during the initial phase. Therefore, while these models were useful for interpreting kinetic trends under controlled conditions, their applicability to real dynamic systems was limited. In summary, the adsorption kinetics were predominantly governed by chemisorption, as indicated by the excellent fit to the PSO model. However, the comparable performance of the Elovich model highlighted the role of surface heterogeneity in the initial adsorption stage. Meanwhile, the weak fit of the IPD model and high C values suggested that boundary layer resistance and pore geometry had a secondary but non-negligible influence on the overall adsorption process.

3.3.3. Adsorption Thermodynamics. The change of enthalpy (ΔH^0), entropy (ΔS^0), and Gibbs free energy (ΔG^0) were determined using eqs 8 and 9 for Cu^{2+}, Ni^{2+}, and Zn^{2+} at four different temperatures under the RSM optimum conditions: 1 g/L, 1000 mg/L, and 36 min for Cu^{2+}; and 1 g/L, 1000 mg/L, and 20 min for both Ni^{2+} and Zn^{2+}. The fitness plot of the thermodynamic model is shown in Figure 10, and the calculated parameter values are listed in Table 6

$$\ln(K_{eq}) = \left(\frac{\Delta S^0}{R}\right) - \left(\frac{\Delta H^0}{R}\right)\left(\frac{1}{T}\right) \quad (8)$$

$$\Delta G^0 = \Delta H^0 - T\Delta S^0 \quad (9)$$

Here, K_{eq} is the thermodynamic equilibrium constant (unitless).

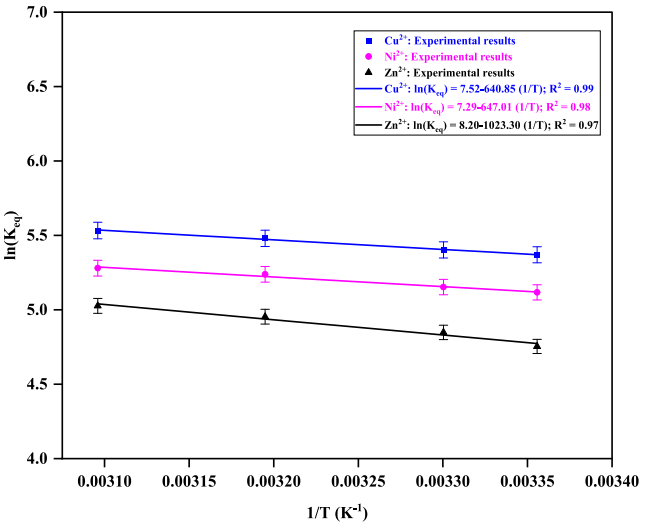

Figure 10. Thermodynamic plots for Cu^{2+}, Ni^{2+}, and Zn^{2+}.

The results indicated that ΔG^0 values were consistently negative (−11.82 to −14.87 kJ/mol) for all three metal ions, suggesting that adsorption on the PGB−CS surface occurred spontaneously.[31] The increasing negativity of ΔG^0 with temperature further implied that the adsorption process became more favorable at higher temperatures due to enhanced mobility and diffusion of metal ions.[31] The positive ΔH^0 values (5.32−8.50 kJ/mol) confirmed that the adsorption

Table 6. Thermodynamic Parameters for Cu^{2+}, Ni^{2+}, and Zn^{2+} Adsorption on PGB−CS

heavy metal	temperature (K)	ΔH^0 (kJ/mol)	ΔS^0 (J mol^{-1} K^{-1})	ΔG^0 (kJ/mol)	R^2
Cu^{2+}	298.15	5.32	62.52	−13.31	0.99
	303.15			−13.62	
	313.15			−14.24	
	323.15			−14.87	
Ni^{2+}	298.15	5.37	60.61	−12.69	0.98
	303.15			−12.99	
	313.15			−13.60	
	323.15			−14.20	
Zn^{2+}	298.15	8.50	68.17	−11.82	0.97
	303.15			−12.16	
	313.15			−12.84	
	323.15			−13.52	

was endothermic in nature. The relatively low enthalpy values likely reflected energetically efficient chemisorptive interactions, particularly outer-sphere complexation or low-energy ion-exchange processes that did not require large activation energy barriers.[21] Moreover, the positive ΔS^0 values (60.61−68.17 J/mol·K) indicated an increase in randomness at the solid−liquid interface during the adsorption process. This entropy gain was likely due to the displacement of water molecules from the hydrated metal ions and the adsorbent surface, resulting in the release of structured water into the bulk solution and thus increasing the overall disorder.[22] The positive ΔS^0 values also implied a greater degree of freedom for the adsorbed species on the surface, which further contributed to the spontaneity of adsorption.[39] Together, these thermodynamic findings revealed that the adsorption of Cu^{2+}, Ni^{2+}, and Zn^{2+} onto the PGB−CS composite was a spontaneous and endothermic process driven by the entropy gain. The thermodynamic observations in this study are aligned with the removal of heavy metals using magnesium chloride-doped *Cicer arietinum* husk biochar,[67] modified fly ash−chitosan composite,[39] and magnetic biochar−chitosan composite.[21]

3.4. Multimetal Removal. *3.4.1. Competitive Adsorption.* The experiments were conducted using a 100 mL solution containing all three metals at a concentration of 200 mg/L, pH 5.0, a duration of 20 min, and a dosage of 1 g/L. The adsorption behavior of binary and ternary systems was investigated and is illustrated in Figure S11. In binary adsorption, removal efficiencies were observed as 84.69% and 62.18% for Cu^{2+} and Ni^{2+}, 89.27% and 68.39% for Cu^{2+} and Zn^{2+}, and 78.90% and 73.04% for Ni^{2+} and Zn^{2+}, respectively. In the ternary system, the removal efficiencies were obtained as 82.36%, 55.91%, and 48.04% for Cu^{2+}, Ni^{2+}, and Zn^{2+}, respectively, highlighting the effectiveness of PGB−CS in concurrently treating multiple metals. The results indicated that Cu^{2+} exhibited higher adsorption capacity compared to Ni^{2+} and Zn^{2+} due to its higher electronegativity (order of electronegativity: $Cu^{2+} > Ni^{2+} > Zn^{2+}$) and smaller ionic size (order of ionic size: $Cu^{2+} < Ni^{2+} < Zn^{2+}$).[68] Similar trends were observed in other studies involving competitive adsorption of heavy metals using cucumber peel adsorbent[69] and modified coal fly ash.[70] In future work, spectroscopic investigations such as XPS deconvolution can be employed to confirm specific interactions between Cu^{2+} and functional groups such as phosphate- or nitrogen-containing moieties. Furthermore, extended studies under binary and ternary metal systems

https://doi.org/10.1021/acsomega.5c04698
ACS Omega XXXX, XXX, XXX−XXX

would provide deeper insights into competitive adsorption mechanisms and selectivity patterns.

3.4.2. Treatment of Industry Effluent. Effluent from a battery manufacturing facility was collected for metal analysis using AAS, revealing concentrations of 800.59 mg/L for Cu^{2+}, 1380.54 mg/L for Ni^{2+}, and 693.56 mg/L for Zn^{2+}, with a solution pH of 5.25. The PGB−CS adsorbent was used at a dosage of 1 g/L for 20 min; removal efficiencies achieved were 83.19%, 61.94%, and 52.34% for Cu^{2+}, Ni^{2+}, and Zn^{2+}, respectively. The results indicated that the PGB−CS adsorbent demonstrated higher selectivity for copper ions compared with those of nickel and zinc ions. Among the three, Cu^{2+} possesses the highest electronegativity and the smallest ionic size, followed by nickel and zinc.[31] Adsorption trends appear to be more favorable for ions with higher electronegativity and smaller ionic radius, as these characteristics enhance the interaction with active sites on the adsorbent surface.[21,39] Consequently, Cu^{2+} displayed a stronger affinity toward the adsorbent, leading to an uptake that was more efficient than those of Ni^{2+} and Zn^{2+}. The native pH of the effluent (5.70) was not adjusted, as it was close to the optimum pH (5.0) determined for the aqueous solution (Section 3.2.3), allowing adsorption to proceed under realistic conditions. Despite this, significant removal efficiencies were achieved, indicating that the PGB−CS performed effectively under uncontrolled pH conditions. Moreover, industrial effluents typically pose a risk of fouling due to the presence of suspended solids, organic matter, or inorganic scaling,[65] while no visible fouling was observed during the batch adsorption cycles. Although the study demonstrated promising performance in treating real effluent, further studies on column operation, along with long-term fouling resistance and cost−benefit analysis, would be necessary to fully evaluate the scalability and operational feasibility of PGB−CS for industrial wastewater treatment. A comparative analysis of adsorbent performance with various studies, summarized in Table 7, demonstrated the potential of the developed PGB−CS for the effective remediation of heavy metal contamination in industrial wastewater.

3.4.3. Effect of Coexisting Ions. The impact of coexisting cations commonly found in wastewater was evaluated through batch adsorption experiments conducted in the presence of Na^+, K^+, Ca^{2+}, and Mg^{2+}, introduced in the form of NaCl, KCl, $CaCl_2$, and $MgCl_2$, respectively. The effects of these coexisting ions on the removal efficiencies of Cu^{2+}, Ni^{2+}, and Zn^{2+} are presented in Figure 11. Each salt was maintained at a concentration of 5 mM (millimolar). The experiments were performed in a separate solution containing Cu^{2+}, Ni^{2+}, and Zn^{2+}, each at an initial concentration of 1000 mg/L, with a PGB−CS dosage of 1 g/L and pH fixed at 5.0. The contact time was varied from 10 to 60 min to investigate the adsorption dynamics in the presence of these competing ions. Monovalent cations (Na^+ and K^+) showed a moderate inhibitory effect on metal removal. At 50 min, the removal efficiency of Cu^{2+} decreased from 94.5% (without ions) to 88.0% with Na^+ and 86.5% with K^+. For Ni^{2+}, the efficiency declined from 82.0% to 76.6% (Na^+) and 75.2% (K^+), while Zn^{2+} removal dropped from 77.5% to 72.4% (Na^+) and 71.4% (K^+). This decline was due to the competition for adsorption sites, although monovalent ions generally exhibit weaker interaction due to their lower charge density and hydration energy.[72] In contrast, the presence of divalent cations (Ca^{2+} and Mg^{2+}) led to a more significant reduction in the removal efficiencies. For Cu^{2+}, the removal efficiency decreased to 81.6% with Ca^{2+} and 78.8% with Mg^{2+}. Similarly, Ni^{2+} removal dropped to 70.3% and 69.0%, while Zn^{2+} decreased to 65.1% and 64.0% in the presence of Ca^{2+} and Mg^{2+}, respectively. These findings suggested a stronger competition from divalent ions, which occupied active sites due to their higher charge.[73] The observed order of interference was $Na^+ < K^+ < Ca^{2+} < Mg^{2+}$, with Zn^{2+} removal being the most adversely affected due to its relatively weaker binding affinity to the functional groups of the PGB−CS. A similar trend of decreasing removal efficiency was observed in the study for the removal of copper ions using polyethylenimine-modified wheat straw.[72]

Table 7. Comparison of Adsorbent Performance for the Heavy Metal Removal from Industry Effluent

adsorbent	effluent type	*Re* (%) Cu^{2+}	*Re* (%) Ni^{2+}	*Re* (%) Zn^{2+}	refs
rice husk	electroplating industry	24.49	94.88	6	30
fly ash	electroplating industry	37.38	94.54	-	30
magnesium oxide nanoparticles	textile and tannery effluent	-	70.80	-	33
peanut husk powder	industry wastewater	51	24	38	71
wood sawdust	electroplating wastewater	38.3	-	14.0	32
polyvinyl alcohol-modified chitosan	battery effluent	79.09	50.73	46.9	31
PGB−CS	battery manufacturing effluent	83.19	61.94	52.34	this study

3.5. Mechanisms of Adsorption. The potential adsorption mechanisms of Cu^{2+}, Ni^{2+}, and Zn^{2+} onto PGB−CS were evaluated based on pH-dependent adsorption behavior, FTIR spectral changes, presence of exchangeable cations, and kinetic modeling data. The pH studies indicated the possible formation of surface precipitates such as $Cu_2Cl(OH)_3$, $Ni(OH)_2(NO_3)$, and $Zn_5(OH)_8Cl_2.H_2O$ during the adsorption of Cu^{2+}, Ni^{2+}, and Zn^{2+}, respectively, suggesting precipitation-assisted removal at higher pH. The FTIR analysis further supported the adsorption mechanisms. Spectra of pristine PGB−CS and metal-loaded forms are shown in Figure 4. The shifts and reduced intensity in the −OH stretching vibrations (3900−3450 to 3850−3387 cm^{-1}) and − COOH-related C═O bands (1625−1460 to 1605−1415 cm^{-1}) indicated surface complexation with metal ions. Additionally, smoother NH_2 peaks (3400−3050 cm^{-1}) and shifts in C═C bands (2450−1950 to 2411−1906 cm^{-1}) suggested electrostatic interactions. The presence of P−O and C−O−P vibrations (notably at 1170 cm^{-1}) confirmed phosphorus functionalization, which could also play a role in metal coordination. Ion exchange was validated by the significant release of native cations such as Mg^{2+}, Ca^{2+}, Na^+, and K^+ into the solution during Cu^{2+}, Ni^{2+}, and Zn^{2+} adsorption, as confirmed by the AAS analysis (Table S3). For example, Mg^{2+} concentration increased from 0.21 to 1.67 mg/L, Ca^{2+} from 0.18 to 1.48 mg/L, Na^+ from 0.26 to 1.94 mg/L, and K^+ from 0.15 to 1.12 mg/L during Cu^{2+} adsorption, indicating displacement of these ions from the adsorbent surface. Similar trends were observed for Mg^{2+}, Ca^{2+}, Na^+, and K^+ during Ni^{2+} and Zn^{2+} adsorption, supporting the involvement of ion exchange in the adsorption mechanism. Kinetic modeling

https://doi.org/10.1021/acsomega.5c04698
ACS Omega XXXX, XXX, XXX−XXX

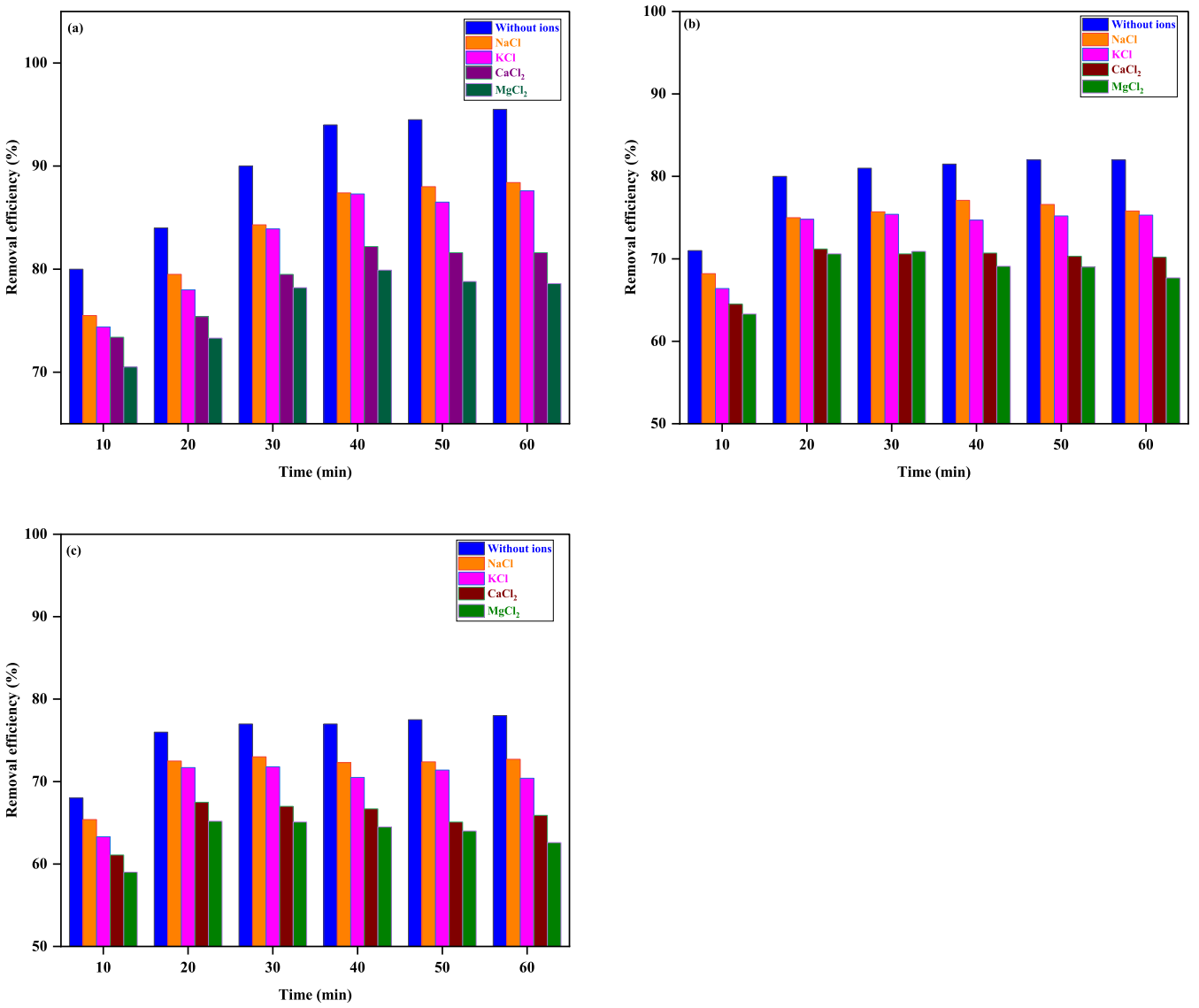

Figure 11. Effect of coexisting ions on the removal efficiency of heavy metals: (a) Cu^{2+} removal, (b) Ni^{2+} removal, and (c) Zn^{2+} removal.

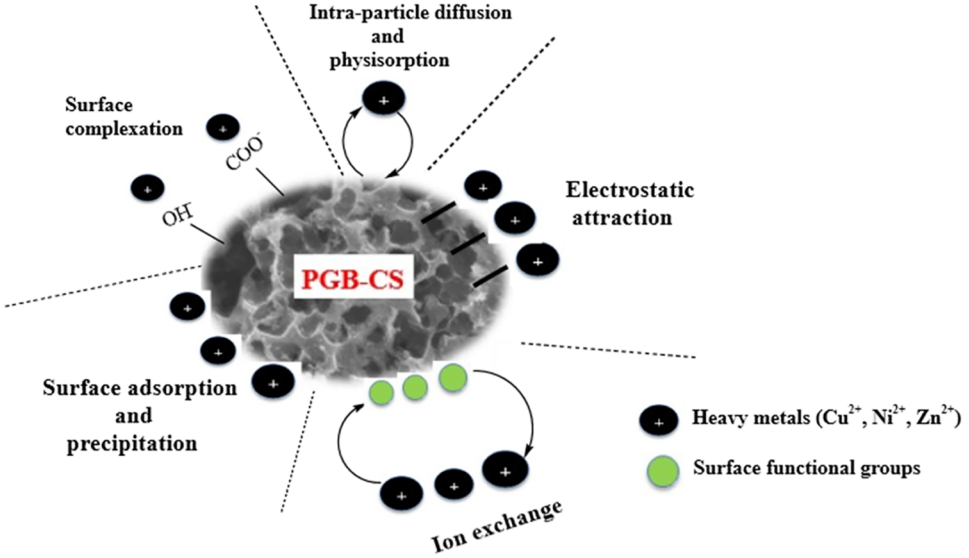

Figure 12. Potential adsorption mechanisms on the PGB−CS surface.

https://doi.org/10.1021/acsomega.5c04698
ACS Omega XXXX, XXX, XXX−XXX

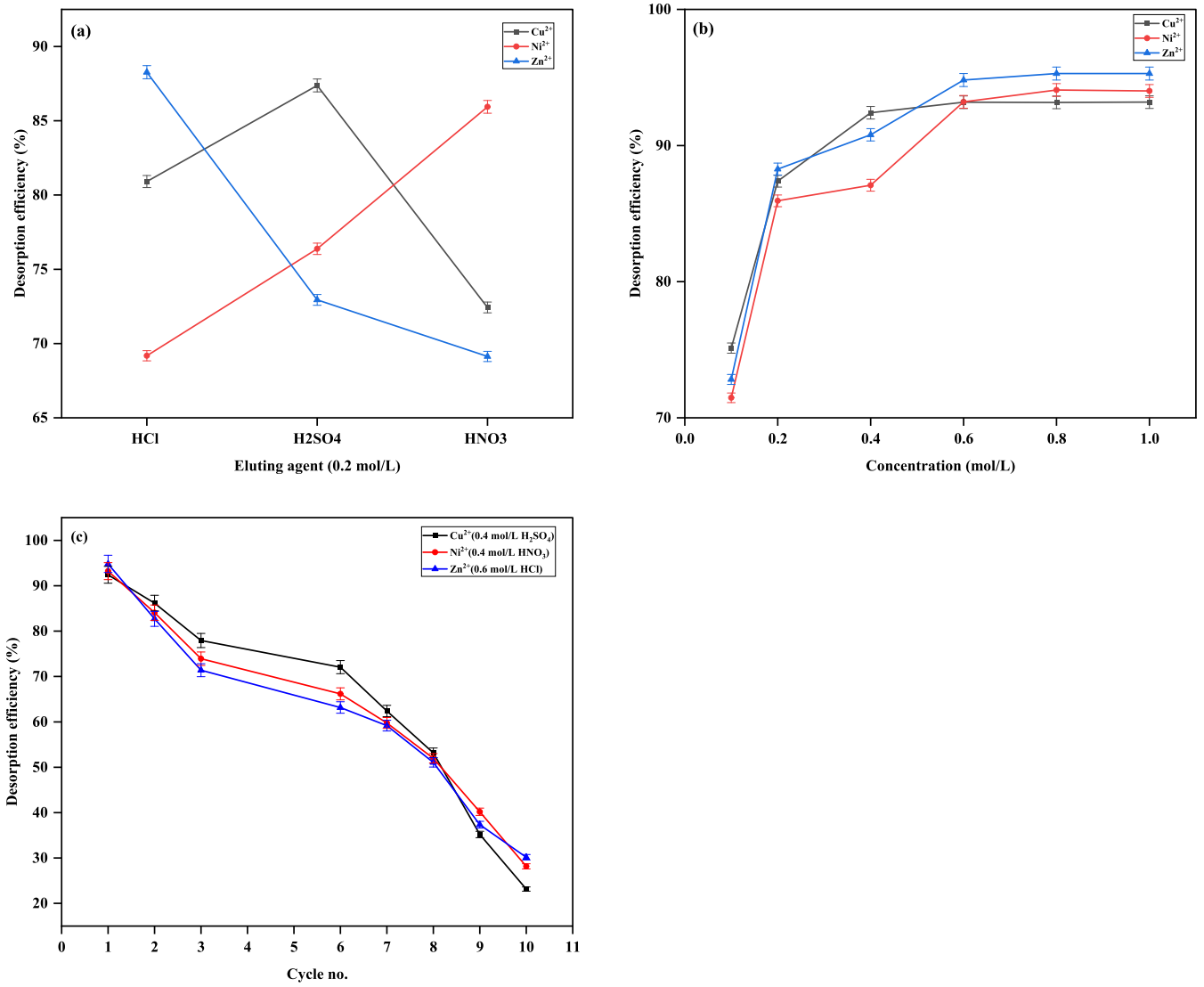

Figure 13. Regeneration study: (a) identification of the eluting agent; (b) determining the optimal eluting agent's concentration; and (c) cyclic performance of PGB−CS.

further indicated that chemisorption was the dominant mechanism, as suggested by the strong fit to the pseudo-second-order (PSO) model and the activation energy (E_a) values from the D−R isotherm model (16−40 kJ/mol). The relatively lower R^2 values (0.69−0.87) from the intraparticle diffusion (IPD) model indicated that diffusion was not the sole rate-controlling step. Based on these observations, the primary adsorption mechanisms were identified as surface complexation, ion exchange, and electrostatic attraction. Similar mechanisms have been reported in the literature for heavy metal removal using poly(vinyl alcohol)-modified chitosan,[31] magnetic biochar−chitosan composite,[21] modified fly ash−chitosan composite,[39] MnO_x-modified biochar,[13] phosphorus/magnesium-engineered biochars,[74] and chitosan-modified bamboo biochar.[75] The graphical representation of potential adsorption mechanisms on the PGB−CS surface is presented in Figure 12.

3.6. Regeneration. The regeneration of the adsorbent is essential for enhancing the sustainability and cost-effectiveness of the adsorption process, as it permits the repeated use of the material.[76] To identify the most effective eluting agent, we tested HCl, H_2SO_4, and HNO_3 at a concentration of 0.2 mol/L and determined the desorption efficiencies for Cu^{2+}, Ni^{2+}, and Zn^{2+} as depicted in Figure 13a. The desorption efficiency (R_{des}) was determined using eq 10

$$R_{des} = \frac{q_{des}}{q_e} \times 100 \quad (10)$$

Here, q_{des} and q_e are the desorption and adsorption capacities (mg/g), respectively.

The results indicated that H_2SO_4 exhibited the highest desorption efficiency for Cu^{2+} (87.38%), HNO_3 for Ni^{2+} (85.94%), and HCl excelled for Zn^{2+} (88.27%) due to anion−metal complexation. Sulfate ions (SO_4^{2-}) were known to form relatively stable complexes with Cu^{2+}, which could have facilitated their enhanced desorption when H_2SO_4 was used.[22] This trend aligned with the earlier observations reported for the regeneration of bentonite−chitosan composite for the copper removal.[22] Similarly, nitrate ions (NO_3^-), which exhibited a higher affinity for Ni^{2+}, could have contributed to the improved elution of Ni^{2+} in the presence of HNO_3, supported by findings from studies involving the bentonite−chitosan composite and pure chitosan for nickel removal,[22,77]

https://doi.org/10.1021/acsomega.5c04698
ACS Omega XXXX, XXX, XXX−XXX

Table 8. Cost Summary of Chemicals and Utility Requirements for the Synthesis of PGB−CS

sr. no.	chemicals/utility	retail cost (Rs.)	quantity required per g for PGB−CS production	cost per g of PGB−CS production (Rs.)
1	high-molecular-weight chitosan	9100 per 100 g	6 g	546
3	acetic acid	406 per 500 mL	6 mL	4.87
4	glutaraldehyde	515 per 500 mL	20 mL	20.6
5	sodium hydroxide	350 per 500 g	6 g	4.20
6	phosphoric acid	550 for 500 mL	15	16.5
6	electricity cost for drying in a hot air oven	10 per KWh	3 units	30
7	electricity cost for DI water purifier	10 per KWh	3 units	30
8	electricity cost for mixing in an orbital shaker	10 per KWh	3 units	30

whereas chloride ions (Cl^-) proved more effective in mobilizing Zn^{2+}, possibly due to the relatively weaker binding affinity of Zn^{2+} to the adsorbent surface and enhanced ion exchange promoted by Cl^- ions at active adsorption sites, aligned with the study of Zn^{2+} desorption using chitosan−magnetic biochar composite.[21] Further optimization was performed by varying the concentrations of H_2SO_4, HNO_3, and HCl from 0.1 to 1 mol/L. The highest desorption efficiency (R_{des}) was achieved at 0.4 mol/L for Cu^{2+} using H_2SO_4 (92.41%), 0.6 mol/L for Ni^{2+} using HNO_3 (93.21%), and 0.6 mol/L for Zn^{2+} using HCl (94.81%), as shown in Figure 13b. At higher concentrations, eluting agents potentially desorbed not only the target metals but also other weakly bound species on the adsorbent, which reduced the overall R_{des}.[78] Afterward, cyclic experiments were conducted using HCl (0.6 mol/L), HNO_3 (0.6 mol/L), and H_2SO_4 (0.4 mol/L) for Zn^{2+}, Ni^{2+}, and Cu^{2+}, respectively (Figure 13c). The PGB−CS demonstrated impressive desorption performance, maintaining 77.93% and 53.17% desorption efficiencies after the third and eighth cycles using H_2SO_4 for Cu^{2+} removal, 73.91% and 51.97% after the third and eighth cycles using HNO_3 for Ni^{2+} removal, and 71.39% and 51.07% after the third and eighth cycles using HCl for Zn^{2+} removal.

To further assess the long-term reusability of PGB−CS, additional regeneration cycles were performed beyond the eighth cycle. The desorption efficiency declined to 35.19%, 40.18%, and 37.34% after the ninth cycle and further to 23.16%, 28.16%, and 30.17% after the 10th cycle for Cu^{2+}, Ni^{2+}, and Zn^{2+}, respectively. This trend indicated a progressive loss of desorption efficiency with repeated use due to the gradual degradation of active sites, pore collapse, structural fatigue, irreversible metal binding, or loss of active functional groups.[39,79] While over 50% efficiency was retained up to the eighth cycle, the sharp drop in subsequent cycles suggested that the practical reusability of PGB−CS should be limited up to the eighth regeneration cycle under the tested conditions. Though stability up to 8 cycles is reasonably good, there is a strong need for more focused studies to enhance the stability and longevity of the adsorbent system under real conditions through appropriate material and process design. The BET analysis of the PGB−CS was conducted after the first, second, fourth, sixth, and eighth regeneration cycles to investigate the decline in the desorption efficiency observed during the cyclic regeneration study. The results, summarized in Table S7, showed a consistent and progressive reduction in surface area, pore diameter, and pore volume with each successive cycle. For example, in the case of Cu^{2+} adsorption, the surface area of PGB−CS decreased from 49.87 m^2/g in cycle 1 to 15.06 m^2/g in cycle 8. Correspondingly, the pore diameter reduced from 4.95 to 2.60 nm and the pore volume declined from 0.215 cm^3/g to 0.10 cm^3/g. Similar trends were observed for the Ni^{2+} and Zn^{2+} removal. These results confirmed that the repeated usage of the adsorbent led to partial pore collapse and structural degradation of the adsorbent, which in turn reduced the availability and accessibility of active sites for metal uptake.[21,39] While over 50% efficiency was retained up to the eighth cycle, the sharp drop in subsequent cycles suggested that the practical reusability of PGB−CS was limited beyond eight regenerations under the tested conditions. To improve long-term performance, alternative regeneration strategies could be explored, such as employing different eluent systems (e.g., EDTA, oxalic acid), introducing mild oxidants (e.g., hydrogen peroxide, $KMnO_4$) to disrupt strong metal−ligand interactions, and optimizing temperature during the desorption. These results emphasized the need for further structural and chemical stability assessments if the material is employed in long-term or column operations.

3.7. Environmental Considerations. Phosphoric acid was used as an activating agent during the synthesis of the PGB−CS composite to improve the surface area, porosity, and functionalization of the biochar. However, the use of phosphoric acid can pose environmental concerns particularly related to its acidic nature.[80,81] To mitigate these effects, the synthesis process was carried out under controlled laboratory conditions, ensuring precise dosing and pH-neutralization. FTIR results confirmed that the presence of phosphate-related functional groups suggested that phosphoric acid was successfully bonded to the PGB−CS surface. Following synthesis, the adsorbent was thoroughly washed until a neutral pH was reached, thereby minimizing the risk of free acid or phosphate leaching into the environment. Moreover, controlled handling of the adsorption process and neutralization of acidic waste before disposal could significantly reduce the environmental risks associated with its use. Additionally, the spent adsorbent, enriched with phosphate groups, could be explored for secondary applications such as soil conditioning, further supporting a circular and sustainable approach.

3.8. Cost Analysis. The retail cost breakdown for various chemicals and utilities required in the synthesis of PGB−CS is detailed in Table 8.

The analysis revealed that producing 1 g of adsorbent costs Rs. 682.14, with chitosan making up a significant 80.12% of the total cost. This emphasizes the importance of reducing chitosan expenses through targeted research and development to lower the overall production cost of PGB−CS.

A cost comparison of various adsorbents used for heavy metal removal is summarized in Table S8, focusing on both the production cost per gram and the cost per mg-metal-removed. The phosphoric acid-modified biochar−chitosan composite (PGB−CS) developed in this study showed a production cost

https://doi.org/10.1021/acsomega.5c04698
ACS Omega XXXX, XXX, XXX−XXX

of 682.14 INR/g, with corresponding metal removal costs of 2.73 INR/mg for Cu^{2+}, 3.56 INR/mg for Ni^{2+}, and 4.67 INR/mg for Zn^{2+}. These values were within the range of other chitosan-based adsorbents such as the phosphoric acid-modified bentonite−chitosan composite (855.61 INR/g; Cu^{2+}: 2.95 INR/mg, Ni^{2+}: 3.86 INR/mg, Zn^{2+}: 4.95 INR/mg) and the chitosan−magnetic cotton husk biochar composite (868.93 INR/g; Zn^{2+}: 7.39 INR/mg). In contrast, biochar from cherry kernels had a lower production cost (239.89 INR/g) but a comparable removal cost for Ni^{2+} (3.62 INR/mg). Synthetic resins such as Purolite C100 and the lignin-based resin from sodium lignosulfonate (SLS) had much lower production costs (3.90 and 2.25 INR/g, respectively) and significantly lower cost per mg of metal removal, particularly in the case of the SLS resin (Cu^{2+}: 0.037 INR/mg, Ni^{2+}: 0.053 INR/mg). While the current cost analysis (Table 8) considered only the direct expenses related to chemicals and electricity, future studies could incorporate additional parameters, such as labor, equipment depreciation, infrastructure, and waste treatment, to obtain a comprehensive understanding of the production economics. The chitosan contributed the maximum cost, sourcing chitosan from crustacean shell waste or other low-cost biopolymer alternatives that could substantially reduce the synthesis cost. Moreover, strategies such as covalent immobilization could be investigated to minimize leaching and improve adsorbent stability over multiple regeneration cycles.

4. CONCLUSIONS

In conclusion, PGB−CS has been demonstrated as an efficient and low-cost adsorbent for the removal of Cu^{2+}, Ni^{2+}, and Zn^{2+} from both aqueous and industrial wastewaters. The pyrolysis conditions of biochar synthesis were optimized to 550 °C for 2 h, which resulted in the enhanced porous structure of the adsorbent. The high adsorption capacities were observed as 249.78 mg/g for Cu^{2+}, 191.48 mg/g for Ni^{2+}, and 145.91 mg/g for Zn^{2+} through three levels of optimization. The abundant functional groups, such as amino, hydroxyl, carboxyl, etc., on the surface of PGB−CS, served as active binding sites for metal ions and facilitated surface complexation and ion-exchange interactions. The adsorption kinetics followed a pseudo-second-order model, indicating that the rate-limiting step was chemisorption between the PGB−CS and metal ions. The fit to the Langmuir isotherm suggested monolayer adsorption on the adsorbent surface. Furthermore, the PGB−CS demonstrated notable stability and reusability, retaining considerable desorption efficiency up to the eighth regeneration cycles, which emphasized its potential for sustainable operation. These findings confirmed that the tailored surface chemistry, high surface area, and functional group availability of PGB−CS were the key contributors to its superior performance. Therefore, PGB−CS holds significant potential for wastewater treatment applications. Future research can be directed toward column studies designed to mimic industrial adsorption systems along with real-time field validation to evaluate long-term operational feasibility. However, several challenges remain before large-scale implementation such as pressure drop across the packed bed, channeling due to irregular flow paths, maintaining a uniform contact time despite the rapid adsorption kinetics, wall and roughness effects, clogging due to the fine particles, bed compaction over prolonged usage due to the swelling or shrinkage of the adsorbent material, etc., which could affect the system performance. Further investigations can be performed to enhance regeneration efficiency, evaluate the reusability of the adsorbent under varying effluent conditions, assess metal recovery and codesorption of competing ions after desorption, assess component leaching and stability over multiple cycles, detailed technoeconomic assessment at scale, use of cheaper alternatives like crustacean waste-derived chitosan, and potential of covalent immobilization to reduce leaching and improve reusability.

■ ASSOCIATED CONTENT

Supporting Information

The Supporting Information is available free of charge at https://pubs.acs.org/doi/10.1021/acsomega.5c04698.

Property comparison of chitosan-based adsorbents for heavy metal removal (Table S1); statistical elemental analysis of PGB−CS before and post adsorption of Cu^{2+}, Ni^{2+}, and Zn^{2+} (Table S2); concentration of exchangeable cations (mg/L) released from PGB−CS before and after adsorption of metal ions (Table S3); statistical analysis of GB at the different pyrolysis temperatures (Table S4); lack-of-fit tests in RSM studies (Table S5); error analysis for repeated experiments in RSM (Table S6); BET study for the cyclic regeneration of PGB−CS (Table S7); cost comparison for heavy metal removal using different adsorbents vis-à-vis reported (Table S8); (a) TGA spectra of PGB−CS, PGB−CS−Cu^{2+}, PGB−CS−Ni^{2+}, and PGB−CS−Zn^{2+}; (b) DTG spectra of PGB−CS, PGB−CS−Cu^{2+}, PGB−CS−Ni^{2+}, and PGB−CS−Zn^{2+} (Figure S1); XRD spectra of (a) PGB−CS, (b) PGB−CS−Cu^{2+}, (c) PGB−CS−Ni^{2+}, and (d) PGB−CS−Zn^{2+} (Figure S2); XPS results of (a) C 1s (after Cu^{2+} adsorption), (b) C 1s (after Ni^{2+} adsorption), (c) C 1s (after Zn^{2+} adsorption), (d) O 1s (after Cu^{2+} adsorption), (e) O 1s (after Ni^{2+} adsorption), (f) O 1s (after Zn^{2+} adsorption), (g) N 1s (after Cu^{2+} adsorption), (h) N 1s (after Ni^{2+} adsorption), and (i) N 1s (after Zn^{2+} adsorption) (Figure S3); residuals and predicted q_e for (a) Cu^{2+}, (b) Ni^{2+}, and (c) Zn^{2+} (Figure S4); predicted vs actual q_e for (a) Cu^{2+}, (b) Ni^{2+}, and (c) Zn^{2+} (Figure S5); 3D surface to study the effects of binary factors on q_e for Cu^{2+}: (a) metal concentration and time, (b) dosage and time, and (c) metal concentration and dosage (Figure S6); 3D surface to study the effects of binary factors on q_e for Ni^{2+}: (a) metal concentration and time, (b) dosage and time, and (c) metal concentration and dosage (Figure S7); 3D surface to study the effects of binary factors on q_e for Zn^{2+}: (a) metal concentration and time, (b) dosage and time, and (c) metal concentration and dosage (Figure S8); normal probability plots of residuals: (a) Cu^{2+}, (b) Ni^{2+}, and (c) Zn^{2+} (Figure S9); effect of various parameters on the removal efficiency of Cu^{2+}, Ni^{2+}, and Zn^{2+}: (a) effect of time, (b) effect of initial metal concentration, and (c) effect of adsorbent dosage (Figure S10); and competitive adsorption of Cu^{2+}, Ni^{2+}, and Zn^{2+} on the PGB−CS adsorbent (Figure S11) (PDF)

■ AUTHOR INFORMATION

Corresponding Author

Inkollu Sreedhar − *Department of Chemical Engineering, Birla Institute of Technology & Science, Pilani, Hyderabad*

https://doi.org/10.1021/acsomega.5c04698
ACS Omega XXXX, XXX, XXX−XXX

500078, India; orcid.org/0000-0003-1706-5735; Phone: +91 4066303512; Email: isreedhar@hyderabad.bits-pilani.ac.in; Fax: +91 4066303998

Author

Khandgave Santosh Sopanrao − *Department of Chemical Engineering, Birla Institute of Technology & Science, Pilani, Hyderabad 500078, India*

Complete contact information is available at: https://pubs.acs.org/10.1021/acsomega.5c04698

Author Contributions

K.S.S.: investigation, methodology, and writing—original draft. I.S.: conceptualization, supervision, validation, resources, writing—review and editing, and project administration.

Notes

The authors declare no competing financial interest.

■ ACKNOWLEDGMENTS

The authors extend their appreciation to the Birla Institute of Technology and Science, Hyderabad campus, for providing the necessary facilities and technical staff of the central analytical lab for facilitating this work.

■ REFERENCES

(1) Lim, A. P.; Aris, A. Z. A Review on Economically Adsorbents on Heavy Metals Removal in Water and Wastewater. *Rev. Environ. Sci. Biotechnol.* **2014**, *13* (2), 163−181.

(2) Patel, P. K.; Pandey, L. M.; Uppaluri, R. V. S. Highly Effective Removal of Multi-Heavy Metals from Simulated Industrial Effluent through an Adsorption Process Employing Carboxymethyl-Chitosan Composites. *Environ. Res.* **2024**, *240* (P1), No. 117502.

(3) Haryanto, B.; Trisakti, B.; Lubis, M.; Tarigan, M. B.; Ketaren, F. Y.; Alexander, V. The Utilization of Pimping Grass (Themeda Gigantea) As Adsorbent of Babura River Water Turbidity With Batch Operation. *Water Conserv. Manage.* **2023**, *8* (1), 54−65.

(4) Azimi, A.; Azari, A.; Rezakazemi, M.; Ansarpour, M. Removal of Heavy Metals from Industrial Wastewaters: A Review. *ChemBioEng Rev.* **2017**, *4* (1), 37−59.

(5) Barakat, M. A. New Trends in Removing Heavy Metals from Industrial Wastewater. *Arab. J. Chem.* **2011**, *4* (4), 361−377.

(6) Sireesha, S.; Sreedhar, I.Unleashing the Potential of Cajanus Cajun Biochar Polymer Composite for Cu (II) Removal: Mechanism, Modification, and Application *Environ. Sci. Pollut. Res.* 2024 DOI: 10.1007/s11356-024-33551-z.

(7) Tian, D.; Xu, Z.; Zhang, D.; Chen, W.; Cai, J.; Deng, H.; Sun, Z.; Zhou, Y. Micro-Mesoporous Carbon from Cotton Waste Activated by $FeCl_3/ZnCl_2$: Preparation, Optimization, Characterization and Adsorption of Methylene Blue and Eriochrome Black T. *J. Solid State Chem.* **2019**, *269*, 580−587.

(8) Maroušek, J.; Trakal, L. Techno-Economic Analysis Reveals the Untapped Potential of Wood Biochar. *Chemosphere* **2022**, *291*, No. 133000.

(9) Qiu, B.; Tao, X.; Wang, H.; Li, W.; Ding, X.; Chu, H. Biochar as a Low-Cost Adsorbent for Aqueous Heavy Metal Removal: A Review. *J. Anal. Appl. Pyrolysis* **2021**, *155*, No. 105081.

(10) Khandgave, S. S.; Sreedhar, I. A Mini-Review on Engineered Biochars as Emerging Adsorbents in Heavy Metal Removal. *Mater. Today Proc.* **2023**, *72*, 19−26.

(11) Li, C.; Wei, H.; Hua, R.; He, X.; Lu, J.; Chen, Q.; Liu, B.; Li, X.; Wu, J. 3D Cu-BTC Anchored on 2D MXene Nanosheets Using Surface Control Approach for Urea Adsorption to Achieve the Regeneration of Dialysate. *Sep. Purif. Technol.* **2025**, *373*, No. 133594.

(12) Patel, P. K. P. K.; Pandey, L. M. L. M.; Uppaluri, R. V. S. Adsorptive Removal of Zn, Fe, and Pb from Zn Dominant Simulated Industrial Wastewater Solution Using Polyvinyl Alcohol Grafted Chitosan Variant Resins. *Chem. Eng. J.* **2023**, *459*, No. 141563.

(13) Santosh, K.; Sarthak, S.; Sadamanti, G.; Utkarsh, S.; Inkollu, U. Enhanced Removal of Cu (II) and Ni (II) Using MnO_x-Modified Non-Edible Biochar : Synthesis, Characterization, Optimization, Thermo-Kinetics, and Regeneration. *Biomass Convers. Biorefin.* **2023**, *14*, 21939−21961.

(14) Zhang, L.; Tang, S.; He, F.; Liu, Y.; Mao, W.; Guan, Y. Highly Efficient and Selective Capture of Heavy Metals by Poly(Acrylic Acid) Grafted Chitosan and Biochar Composite for Wastewater Treatment. *Chem. Eng. J.* **2019**, *378*, No. 122215.

(15) Hidayat, E.; Yoshino, T.; Yonemura, S.; Mitoma, Y.; Harada, H. A Carbonized Zeolite/Chitosan Composite as an Adsorbent for Copper (II) and Chromium (VI) Removal from Water. *Materials* **2023**, *16* (6), No. 2532.

(16) Yu, J.; Zheng, J.; Lu, Q.; Yang, S.; Zhang, X.; Wang, X.; Yang, W. Selective Adsorption and Reusability Behavior for Pb^{2+} and Cd^{2+} on Chitosan/Poly(Ethylene Glycol)/Poly(Acrylic Acid) Adsorbent Prepared by Glow-Discharge Electrolysis Plasma. *Colloid Polym. Sci.* **2016**, *294* (10), 1585−1598.

(17) Zhu, C.; Liu, F.; Zhang, Y.; Wei, M.; Zhang, X.; Ling, C.; Li, A. Nitrogen-Doped Chitosan-Fe(III) Composite as a Dual-Functional Material for Synergistically Enhanced Co-Removal of Cu(II) and Cr(VI) Based on Adsorption and Redox. *Chem. Eng. J.* **2016**, *306*, 579−587.

(18) Luo, W.; Bai, Z.; Zhu, Y. Fast Removal of Co(ii) from Aqueous Solution Using Porous Carboxymethyl Chitosan Beads and Its Adsorption Mechanism. *RSC Adv.* **2018**, *8* (24), 13370−13387.

(19) Sethy, T. R. T. R.; Pradhan, A. K. A. K.; Sahoo, P. K. P. K. Simultaneous Studies on Kinetics, Bio-Adsorption Behaviour of Chitosan Grafted Thin Film Nanohydrogel for Removal of Hazardous Metal Ion from Water. *Environ. Nanotechnol., Monit. Manage.* **2019**, *12*, No. 100262.

(20) Verma, R.; Asthana, A.; Singh, A. K.; Prasad, S. An Arginine Functionalized Magnetic Nano-Sorbent for Simultaneous Removal of Three Metal Ions from Water Samples. *RSC Adv.* **2017**, *7* (81), 51079−51089.

(21) Sopanrao, K. S.; Sreedhar, I. Sustainable Zn2+ Removal Using Highly Efficient, Novel, and Cost-Effective Chitosan-Magnetic Biochar Composite. *Environ. Sci. Pollut. Res.* **2024**, No. 0123456789.

(22) Sopanrao, K. S.; Venugopal, A.; Patel, C. M.; Sreedhar, I. Phosphoric Acid−Modified Bentonite-Chitosan Composite Beads: A Novel and Cost-Effective Adsorbent for Multi-Metal Wastewater Treatment. *Environ. Sci. Pollut. Res.* **2024**, No. 0123456789.

(23) Zhou, L.; Chen, L.; Zhang, Y.; Zhang, Y.; Li, Z.; Yang, K.; Chen, L. The Adsorption Characteristics of Phosphorus-Modified Corn Stover Biochar on Lead and Cadmium. *Agriculture* **2024**, *14* (7), No. 1118.

(24) Amuda, O. S. S.; Giwa, A. A. A.; Bello, I. A. A. Removal of Heavy Metal from Industrial Wastewater Using Modified Activated Coconut Shell Carbon. *Biochem. Eng. J.* **2007**, *36* (2), 174−181.

(25) Yang, C.; Yao, Q.; Li, L.; Xiao, X.; Lu, L.; Liu, C.; Zhu, C.; Zhan, S.; Yuan, H. The Isolated Ca-Nx Sites in Biochar Boosting Fe Catalyzed Fenton-like Oxidation of Tris(2-Chloroethyl) Phosphate: Properties, Mechanisms, and Applications. *Appl. Catal., B* **2025**, *366*, No. 125056.

(26) Mahmoud, S. A.; Atia, B. M.; Abdalla, M. Polyvinyl Alcohol-Conjugated L-Cysteine: A Novel Metal Pincer for Efficient Heavy Metal Ions Removal from Wastewater. *ChemistrySelect* **2024**, *9* (26), No. e202401169.

(27) A, J.; Al-Jawaldeh, H.; Al-Zghoul, T. M.; Hamaideh, A.; Darwish, M. M.; Al-Karablieh, E. Olive Pits Activated Carbon As an Effective Adsorbent for Water Treatment Using H_3PO_4 and H_2SO_4 Activating Agents. *Water Conserv. Manage.* **2024**, *8* (4), 415−419.

(28) Mahmoud, S. A.; Atia, B. M.; Gado, M. A. Efficient Removal of Toxic Metals (Hg(II), Cr(III), Pb(II), Cd(II)) Using High-Performance Polyvinyl Alcohol-L-2-Amino-3-Mercaptopropionic Acid Composite from Wastewater. *Int. J. Environ. Sci. Technol.* **2025**, *22* (13), 12269−12294.

(29) El Mansouri, F.; El Farissi, H.; Cacciola, F.; Talhaoui, A.; El Bachiri, A.; Tahani, A.; Esteves da Silva, J. C. G.; Brigui, J. Rapid Elimination of Copper (II), Nickel (II) and Chromium (VI) Ions from Aqueous Solutions by Charcoal Modified with Phosphoric Acid Used as a Green Biosorbent. *Polym. Adv. Technol.* **2022**, *33* (7), 2254−2264.
(30) Hegazi, H. A. Removal of Heavy Metals from Wastewater Using Agricultural and Industrial Wastes as Adsorbents. *HBRC J.* **2013**, *9* (3), 276−282.
(31) Sopanrao, K. S.; Sreedhar, I. Polyvinyl Alcohol Modified Chitosan Composite as a Novel and Efficient Adsorbent for Multi-Metal Removal. *Sep. Purif. Technol.* **2024**, *340*, No. 126731.
(32) Šćiban, M.; Radetić, B.; Kevrešan, Ž.; Klašnja, M. Adsorption of Heavy Metals from Electroplating Wastewater by Wood Sawdust. *Bioresour. Technol.* **2007**, *98* (2), 402−409.
(33) Fouda, A.; Hassan, S. E. D.; Saied, E.; Hamza, M. F. Photocatalytic Degradation of Real Textile and Tannery Effluent Using Biosynthesized Magnesium Oxide Nanoparticles (MgO-NPs), Heavy Metal Adsorption, Phytotoxicity, and Antimicrobial Activity. *J. Environ. Chem. Eng.* **2021**, *9* (4), No. 105346.
(34) Siddiqui, S.; Bhatnagar, P.; Sireesha, S.; Sopanrao, K. S.; Sreedhar, I. Efficient Copper Removal Using Low-Cost H_3PO_4 Impregnated Red-Gram Biochar-MnO_2 Nanocomposites. *Bioresour. Technol. Rep.* **2023**, *21*, No. 101304.
(35) Anirudhan, T. S. S.; Lekshmi, G. S. S.; Shainy, F. Synthesis and Characterization of Amidoxime Modified Chitosan/Bentonite Composite for the Adsorptive Removal and Recovery of Uranium from Seawater. *J. Colloid Interface Sci.* **2019**, *534*, 248−261.
(36) Chen, H.; Gao, Y.; El-Naggar, A.; Niazi, N. K.; Sun, C.; Shaheen, S. M.; Hou, D.; Yang, X.; Tang, Z.; Liu, Z.; Hou, H.; Chen, W.; Rinklebe, J.; Pohořelý, M.; Wang, H. Enhanced Sorption of Trivalent Antimony by Chitosan-Loaded Biochar in Aqueous Solutions: Characterization, Performance and Mechanisms. *J. Hazard. Mater.* **2022**, *425*, No. 127971.
(37) Bąk, J.; Thomas, P.; Kołodyńska, D. Chitosan-Modified Biochars to Advance Research on Heavy Metal Ion Removal: Roles, Mechanism and Perspectives. *Materials* **2022**, *15* (17), No. 6108.
(38) Mousavi, S. J.; Parvini, M.; Ghorbani, M. Adsorption of Heavy Metals (Cu^{2+} and Zn^{2+}) on Novel Bifunctional Ordered Mesoporous Silica: Optimization by Response Surface Methodology. *J. Taiwan Inst. Chem. Eng.* **2018**, *84*, 123−141.
(39) Sopanrao, K. S.; Sreedhar, I. Novel Coal Flyash-Chitosan Composite for Highly Efficient, Cost-Effective and Stable Removal of Lead and Chromium from Industrial Wastewater. *Environ. Sci. Water Res. Technol.* **2025**, *11*, 1977−2001.
(40) Dechapanya, W.; Khamwichit, A. Biosorption of Aqueous Pb(II) by H_3PO_4-Activated Biochar Prepared from Palm Kernel Shells (PKS). *Heliyon* **2023**, *9* (7), No. 17250.
(41) Sireesha, S.; Sreedhar, I. Holistic and Parametric Optimization Study on Cr(VI) Removal Using Acid-Treated Coco Peat Biochar Adsorbent. *Bioresour. Technol. Rep.* **2023**, *22*, No. 101486.
(42) Yang, Y.; Zhang, Y.; Wang, G.; Yang, Z.; Xian, J.; Yang, Y.; Li, T.; Pu, Y.; Jia, Y.; Li, Y.; Cheng, Z.; Zhang, S.; Xu, X. Adsorption and Reduction of Cr(VI) by a Novel Nanoscale FeS/Chitosan/Biochar Composite from Aqueous Solution. *J. Environ. Chem. Eng.* **2021**, *9* (4), No. 105407.
(43) Zhang, H.; Li, R.; Zhang, Z. A Versatile EDTA and Chitosan Bi-Functionalized Magnetic Bamboo Biochar for Simultaneous Removal of Methyl Orange and Heavy Metals from Complex Wastewater. *Environ. Pollut.* **2022**, *293*, No. 118517.
(44) Chen, S.; Zhong, M.; Wang, H.; Zhou, S.; Li, W.; Wang, T.; Li, J. Study on Adsorption of Cu^{2+}, Pb^{2+}, Cd^{2+}, and Zn^{2+} by the $KMnO_4$ Modified Biochar Derived from Walnut Shell. *Int. J. Environ. Sci. Technol.* **2023**, *20* (2), 1551−1568.
(45) Li, W.; Guo, M.; Wang, Y.; Deng, H.; Lei, H.; Yu, C.; Liu, Z. Selective Adsorption of Heavy Metal Ions by Different Composite-Modified Semi-Carbonized Fibers. *Sep. Purif. Technol.* **2024**, *328*, No. 125022.
(46) Xu, Y.; Bai, T.; Li, Q.; Yang, H.; Yan, Y.; Sarkar, B.; Lam, S. S.; Bolan, N. Influence of Pyrolysis Temperature on the Characteristics and Lead(II) Adsorption Capacity of Phosphorus-Engineered Poplar Sawdust Biochar. *J. Anal. Appl. Pyrolysis* **2021**, *154*, No. 105010.
(47) Huang, X.; Zhao, H.; Hu, X.; Liu, F.; Wang, L.; Zhao, X.; Gao, P.; Ji, P. Optimization of Preparation Technology for Modified Coal Fly Ash and Its Adsorption Properties for Cd^{2+}. *J. Hazard. Mater.* **2020**, *392*, No. 122461.
(48) Zaferani, S. P. G.; Emami, M. R. S.; Amiri, M. K.; Binaeian, E. Optimization of the Removal Pb (II) and Its Gibbs Free Energy by Thiosemicarbazide Modified Chitosan Using RSM and ANN Modeling. *Int. J. Biol. Macromol.* **2019**, *139*, 307−319.
(49) Sakhiya, A. K.; Baghel, P.; Anand, A.; Vijay, V. K.; Kaushal, P. A Comparative Study of Physical and Chemical Activation of Rice Straw Derived Biochar to Enhance Zn^{+2} Adsorption. *Bioresour. Technol. Rep.* **2021**, *15*, No. 100774, DOI: 10.1016/j.biteb.2021.100774.
(50) Burk, G. A.; Herath, A.; Crisler, G. B.; Bridges, D.; Patel, S.; Pittman, C. U.; Mlsna, T. Cadmium and Copper Removal From Aqueous Solutions Using Chitosan-Coated Gasifier Biochar. *Front. Environ. Sci.* **2020**, *8*, No. 541203, DOI: 10.3389/fenvs.2020.541203.
(51) López, J.; Loida, L.; Montes, E. R.; Martinez, S.; Arturo, V. Linear and Nonlinear Kinetic and Isotherm Adsorption Models for Arsenic Removal by Manganese Ferrite Nanoparticles. *SN Appl. Sci.* **2019**, *1* (8), No. 950.
(52) Liu, M.; Almatrafi, E.; Zhang, Y.; Xu, P.; Song, B.; Zhou, C.; Zeng, G.; Zhu, Y. A Critical Review of Biochar-Based Materials for the Remediation of Heavy Metal Contaminated Environment: Applications and Practical Evaluations. *Sci. Total Environ.* **2022**, *806*, No. 150531.
(53) Timur, M.; Paşa, A. Synthesis, Characterization, Swelling, and Metal Uptake Studies of Aryl Cross-Linked Chitosan Hydrogels. *ACS Omega* **2018**, *3* (12), 17416−17424.
(54) Arabyarmohammadi, H.; Darban, A. K.; Abdollahy, M.; Yong, R.; Ayati, B.; Zirakjou, A.; van der Zee, S. E. A. T. M. Utilization of a Novel Chitosan/Clay/Biochar Nanobiocomposite for Immobilization of Heavy Metals in Acid Soil Environment. *J. Polym. Environ.* **2018**, *26* (5), 2107−2119.
(55) Fan, C.; Li, K.; Li, J.; Ying, D.; Wang, Y.; Jia, J. Comparative and Competitive Adsorption of Pb(II) and Cu(II) Using Tetraethylenepentamine Modified Chitosan/$CoFe_2O_4$ particles. *J. Hazard. Mater.* **2017**, *326*, 211−220.
(56) Sahebjamee, N.; Soltanieh, M.; Mousavi, S. M.; Heydarinasab, A. Removal of Cu^{2+}, Cd^{2+} and Ni^{2+} Ions from Aqueous Solution Using a Novel Chitosan/Polyvinyl Alcohol Adsorptive Membrane. *Carbohydr. Polym.* **2019**, *210*, 264−273.
(57) Popuri, S. R.; Vijaya, Y.; Boddu, V. M.; Abburi, K. Adsorptive Removal of Copper and Nickel Ions from Water Using Chitosan Coated PVC Beads. *Bioresour. Technol.* **2009**, *100* (1), 194−199.
(58) Keshvardoostchokami, M.; Babaei, S.; Piri, F.; Zamani, A. Nitrate Removal from Aqueous Solutions by ZnO Nanoparticles and Chitosan-Polystyrene-Zn Nanocomposite: Kinetic, Isotherm, Batch and Fixed-Bed Studies. *Int. J. Biol. Macromol.* **2017**, *101*, 922−930.
(59) Wang, Z.-K.; Ji, J.-R.; Tang, R.; Lu, C.-M.; Yu, S.-S.; Li, D.-D.; Tong, Z.-F.; Zhang, H.-B.; He, M.-Y. Preparation of Dual Organic Modified Magnetic Bentonite for Cu(II) and Zn(II) Adsorption. *J. Chem. Eng. Chin. Univ.* **2022**, *36* (2), 276−286.
(60) Dev, V. V.; Baburaj, G.; Antony, S.; Arun, V.; Krishnan, K. A. Zwitterion-Chitosan Bed for the Simultaneous Immobilization of Zn(II), Cd(II), Pb(II) and Cu(II) from Multi-Metal Aqueous Systems. *J. Cleaner Prod.* **2020**, *255*, No. 120309.
(61) Kusrini, E.; Sofyan, N.; Nurjaya, D. M.; Santoso, S.; Tristantini, D. Removal of Heavy Metals from Aqueous Solution by Hydroxyapatite/Chitosan Composite. *Adv. Mater. Res.* **2013**, *789*, 176−179.
(62) Cheng, S.; Liu, Y.; Xing, B.; Qin, X.; Zhang, C.; Xia, H. Lead and Cadmium Clean Removal from Wastewater by Sustainable Biochar Derived from Poplar Saw Dust. *J. Cleaner Prod.* **2021**, *314*, No. 128074.

https://doi.org/10.1021/acsomega.5c04698
ACS Omega XXXX, XXX, XXX−XXX

(63) Yin, G.; Tao, L.; Chen, X.; Bolan, N. S.; Sarkar, B.; Lin, Q.; Wang, H. Quantitative Analysis on the Mechanism of Cd^{2+} Removal by $MgCl_2$-Modified Biochar in Aqueous Solutions. *J. Hazard. Mater.* **2021**, *420*, No. 126487, DOI: 10.1016/j.jhazmat.2021.126487.
(64) Tan, Y.; Wan, X.; Ni, X.; Wang, L.; Zhou, T.; Sun, H.; Wang, N.; Yin, X. Efficient Removal of Cd(II) from Aqueous Solution by Chitosan Modified Kiwi Branch Biochar. *Chemosphere* **2022**, *289*, No. 133251.
(65) Biswal, B. K.; Vijayaraghavan, K.; Tsen-Tieng, D. L.; Balasubramanian, R. Biochar-Based Bioretention Systems for Removal of Chemical and Microbial Pollutants from Stormwater: A Critical Review. *J. Hazard. Mater.* **2022**, *422*, No. 126886, DOI: 10.1016/j.jhazmat.2021.126886.
(66) Wang, J.; Guo, X. Rethinking of the Intraparticle Diffusion Adsorption Kinetics Model: Interpretation, Solving Methods and Applications. *Chemosphere* **2022**, *309* (P2), No. 136732.
(67) Isaac, R.; Siddiqui, S. Adsorption of Divalent Copper from Aqueous Solution by Magnesium Chloride Co-Doped Cicer Arietinum Husk Biochar: Isotherm, Kinetics, Thermodynamic Studies and Response Surface Methodology. *Bioresour. Technol. Rep.* **2022**, *18*, No. 101004.
(68) Fan, X.; Wang, X.; Cai, Y.; Xie, H.; Han, S.; Hao, C. Functionalized Cotton Charcoal/Chitosan Biomass-Based Hydrogel for Capturing Pb^{2+}, Cu^{2+} and MB. *J. Hazard. Mater.* **2022**, *423*, No. 127191.
(69) Basu, M.; Guha, A. K.; Ray, L. Adsorption of Lead on Cucumber Peel. *J. Cleaner Prod.* **2017**, *151*, 603−615.
(70) Sireesha, S.; Agarwal, A.; Sopanrao, K. S.; Sreedhar, I.; Anitha, K. L. Modified Coal Fly Ash as a Low-Cost, Efficient, Green, and Stable Adsorbent for Heavy Metal Removal from Aqueous Solution. *Biomass Convers. Biorefin.* **2022**, DOI: 10.1007/s13399-022-02695-8.
(71) Abdelfattah, I.; Ismail, A. A.; Al Sayed, F.; Almedolab, A.; Aboelghait, K. M. Biosorption of Heavy Metals Ions in Real Industrial Wastewater Using Peanut Husk as Efficient and Cost Effective Adsorbent. *Environ. Nanotechnol., Monit. Manage.* **2016**, *6*, 176−183.
(72) Dong, J.; Du, Y.; Duyu, R.; Shang, Y.; Zhang, S.; Han, R. Adsorption of Copper Ion from Solution by Polyethylenimine Modified Wheat Straw. *Bioresour. Technol. Rep.* **2019**, *6*, 96−102.
(73) Upadhyay, U.; Sreedhar, I.; Singh, S. A.; Patel, C. M.; Anitha, K. L. Recent Advances in Heavy Metal Removal by Chitosan Based Adsorbents. *Carbohydr. Polym.* **2021**, *251*, No. 117000.
(74) Penido, E. S.; Melo, L. C. A.; Guilherme, L. R. G.; Bianchi, M. L. Cadmium Binding Mechanisms and Adsorption Capacity by Novel Phosphorus/Magnesium-Engineered Biochars. *Sci. Total Environ.* **2019**, *671*, 1134−1143.
(75) Huang, A.; Bai, W.; Yang, S.; Wang, Z.; Wu, N.; Zhang, Y.; Ji, N.; Li, D. Adsorption Characteristics of Chitosan-Modified Bamboo Biochar in Cd(II) Contaminated Water. *J. Chem.* **2022**, No. 6303252.
(76) Hassan, M.; Naidu, R.; Du, J.; Liu, Y.; Qi, F. Critical Review of Magnetic Biosorbents: Their Preparation, Application, and Regeneration for Wastewater Treatment. *Sci. Total Environ.* **2020**, *702*, No. 134893, DOI: 10.1016/j.scitotenv.2019.134893.
(77) Nicomel, N. R.; Otero-Gonzalez, L.; Folens, K.; Mees, B.; Hennebel, T.; Du Laing, G. Selective and Enhanced Nickel Adsorption from Sulfate- and Calcium-Rich Solutions Using Chitosan. *Sep. Purif. Technol.* **2021**, *276*, No. 119283.
(78) Mallik, A. K.; Kabir, S. F.; Bin Abdur Rahman, F.; Sakib, M. N.; Efty, S. S.; Rahman, M. M. Cu(II) Removal from Wastewater Using Chitosan-Based Adsorbents: A Review. *J. Environ. Chem. Eng.* **2022**, *10* (4), No. 108048.
(79) Dutta, T.; Kim, T.; Vellingiri, K.; Tsang, D. C. W.; Shon, J. R.; Kim, K. H.; Kumar, S. Recycling and Regeneration of Carbonaceous and Porous Materials through Thermal or Solvent Treatment. *Chem. Eng. J.* **2019**, *364*, 514−529.
(80) Yin, Q.; Zhang, B.; Wang, R.; Zhao, Z. Biochar as an Adsorbent for Inorganic Nitrogen and Phosphorus Removal from Water: A Review. *Environ. Sci. Pollut. Res.* **2017**, *24*, 26297−26309, DOI: 10.1007/s11356-017-0338-y.
(81) Vikrant, K.; Kim, K. H.; Ok, Y. S.; Tsang, D. C. W.; Tsang, Y. F.; Giri, B. S.; Singh, R. S. Engineered/Designer Biochar for the Removal of Phosphate in Water and Wastewater. *Sci. Total Environ.* **2018**, *616*−*617*, 1242−1260.

https://doi.org/10.1021/acsomega.5c04698
ACS Omega XXXX, XXX, XXX−XXX